

## Article

# An Artificial Network-Based Prediction of Key Reference Zones on Axial Stress–Strain Curves of FRP-Confined Concrete

Ali Fallah Pour<sup>1</sup> and Aliakbar Gholampour<sup>2,\*</sup> <sup>1</sup> School of Civil, Environmental and Mining Engineering, University of Adelaide, Adelaide, SA 5005, Australia<sup>2</sup> College of Science and Engineering, Flinders University, Tonsley, SA 5042, Australia\* Correspondence: [aliakbar.gholampour@flinders.edu.au](mailto:aliakbar.gholampour@flinders.edu.au)

**Abstract:** The accurate prediction of reference points on the axial stress–axial strain relationship of fiber-reinforced polymer (FRP)-confined concrete is vital to pre-design structures made with this system. This study uses an artificial neural network (ANN) for predicting hoop rupture strain ( $\epsilon_{h,rupt}$ ) and transition zone, namely transition strain ( $\epsilon_{c1}$ ) and stress ( $f'_{c1}$ ), on axial stress–strain curves of FRP-confined concrete. These are key parameters for estimating a transition zone of stress–strain curves. In this study, accompanied with these parameters, ultimate condition parameters, including compressive strength and ultimate axial strain, were predicted using a comprehensive database. Various combinations of input data and ANN parameters were used to increase the accuracy of the predictions. A sensitivity analysis and a model validation assessment were performed to evaluate the predictability of the developed models. At the end, a comparison between the proposed models in this study and existing ANN and design-oriented models was presented. It is shown that the accuracy of the developed ANN models in this study is higher or comparable to that of existing ANN models. Additionally, the developed models in this study to predict  $f'_{c1}$  and  $\epsilon_{c1}$  exhibit a higher accuracy compared to existing design-oriented models. These results indicate that the proposed ANN models capture the lateral confinement effect on ultimate and transition zones of FRP-confined concrete with a more robust performance compared to existing models.

**Keywords:** FRP-confined concrete; hoop rupture strain; artificial neural network (ANN); ultimate axial strain; transition zone; compressive strength



**Citation:** Fallah Pour, A.; Gholampour, A. An Artificial Network-Based Prediction of Key Reference Zones on Axial Stress–Strain Curves of FRP-Confined Concrete. *Appl. Sci.* **2023**, *13*, 3038. <https://doi.org/10.3390/app13053038>

Academic Editor: Raffaele Pucinotti

Received: 2 February 2023

Revised: 23 February 2023

Accepted: 25 February 2023

Published: 27 February 2023



**Copyright:** © 2023 by the authors. Licensee MDPI, Basel, Switzerland. This article is an open access article distributed under the terms and conditions of the Creative Commons Attribution (CC BY) license (<https://creativecommons.org/licenses/by/4.0/>).

## 1. Introduction

Fiber-reinforced polymer (FRP) as a confinement material for concrete columns has been investigated by numerous studies for last four decades [1]. Mechanical characteristics of FRP-confined concrete with compressive loading was investigated in-depth, and various models were developed to predict the characteristics of concrete columns confined with FRP tubes. However, the prediction of some reference parameters on stress–strain relationships of this high-performance structural system, such as hoop rupture strain and axial strain at ultimate, still needs a closer examination [2–4]. Additionally, the transition point as another influential zone on the stress–strain curve has not been examined closely, although few studies developed models to predict this key reference point [5–8]. The transition point is an area where the first ascending nonlinear segment of the stress–strain curve links to the second quasi-linear segment [9]. The stress–strain curves after their transition point show different behaviors: ascending or descending trend [3]. As explained by Fallah Pour et al. [4], through accurate estimation of the ultimate and transition zone of FRP-confined concretes, their whole axial stress–strain curve is predicted accurately. In this study, the main area of focus is the curves, which show ascending or descending behavior after the transition zone.

Various approaches, such as analysis-oriented and design-oriented, have been utilized for predicting the characteristics of concretes confined with FRP. Analysis-oriented models

have been versatile models due to their ability in predicting the whole stress–strain curve. However, these models depend significantly on the concrete dilation behavior. Existing predictions for this behavior were either inaccurate or time-consuming due to the need for great computational effort [10–13]. Assessment of existing design-oriented expressions expanded by different studies showed that they could approximately provide accurate predictions for compressive strength ( $f'_{cc}$ ) and axial transition stress ( $f'_{c1}$ ) [4,9]. However, they could not accurately estimate the strain corresponding to  $f'_{cc}$  ( $\varepsilon_{cu}$ ) [4,9]. Furthermore, the existing expressions for  $\varepsilon_{cu}$  prediction used experimental hoop rupture strain ( $\varepsilon_{h,rupt}$ ). However,  $\varepsilon_{h,rupt}$  does not readily exist in designing procedures. Additionally, Bisby et al. [14,15] discussed that the reported experimental  $\varepsilon_{h,rupt}$  had an inconsistency. In addition, some of the experimental data could not follow the trend of  $\varepsilon_{h,rupt}$ . They discussed that this is partly due to location of shear planes and using strain gauges as a measurement method [3,14,15]. Similar to  $\varepsilon_{cu}$  and  $\varepsilon_{h,rupt}$ , accurate estimation of axial strain at the transition zone ( $\varepsilon_{c1}$ ), as another key reference strain, was not possible using existing proposed design-oriented expressions [4]. These observations in the performed literature review indicate that more investigation is essential on the prediction of significant reference strains, namely  $\varepsilon_{cu}$ ,  $\varepsilon_{h,rupt}$ , and  $\varepsilon_{c1}$ .

Data-driven-based methods recently have received a great deal of attention due to their simplicity in use and usually offering a closed-form model for predictions. These models include various types of evaluation algorithms, including artificial neural network (ANN), generic programming (GP), stepwise regression, and fuzzy logic algorithms [16]. Ghaboussi et al. [17] used a neural network as both a knowledge-based and a data-driven technique to predict the characteristics of different materials. Their prediction was developed directly from experimental datasets by ignoring prior assumption and human observations. They discussed that in the analysis of neural network models, the characteristics of materials can be implicitly captured using parameters of weight [17]. Khan et al. [18] developed hybrid ANN models for durability analysis of glass-FRP rebars in an alkaline concrete environment. Zheng et al. [19] predicted the compressive strength of concrete using an ANN mesoscale concretization model. They found that their model could accurately capture the mechanical response of the concrete. Huang et al. [20] developed a back-propagation ANN model to capture the interface bond behavior of FRP-reinforced concrete. Different meta-heuristic algorithms (e.g., particle swarm optimization, social spider optimization) were used by Sarkhani Benemaran et al. [21] to improve the prediction accuracy of a gradient boosting-based method for estimating the resilient modulus of flexible pavement foundations. Finally, Yildizel and Toktas [22] used an artificial bee colony algorithm to design multilayer microwave absorbing foam concrete.

In the case of FRP-confined concrete, Ozbakkaloglu et al. [1] and Jiang et al. [16] reported that numerous predictions were developed using data-driven approaches to estimate the ultimate condition of the confined concrete having a circular-shape cross-section. Ozbakkaloglu et al. [1] reported the existence of more than 88 expressions to predict  $\varepsilon_{cu}$  and  $f'_{cc}$  of confined concretes with FRP. Different studies used ANN and GP to estimate  $\varepsilon_{cu}$  and  $f'_{cc}$  (e.g., [16,23–27]). It was reported that an ANN was able to predict  $f'_{cc}$  more accurately compared to traditional approaches [16]. Wu et al. [28] used the other type of neural network, i.e., radial basis function network, to predict  $f'_{cc}$ . Cascardi et al. [29] determined  $f'_{cc}$  by predicting the efficiency of a FRP jacket using an ANN technique. Recently, Isleem et al. [30] used ANN to build a confinement model to predict the ultimate condition of FRP-confined concrete. However, their model was limited to the test results obtained in their study. Jiang et al. [16] predicted  $\varepsilon_{cu}$  in addition to  $f'_{cc}$  using an ANN accompanied with the prediction of the stress–strain relationship. Similar to the concretes with a circular cross-section, the ultimate condition of the concretes with square and rectangular cross-sections were also examined by ANN analysis in different studies [31–33]. Nonetheless, the literature review revealed that no research has examined the prediction of a transition zone using an ANN. Existing models were either complex, dealt with a small number of databases, or ignored key influential input parameters on the behavior of

FRP-confined concrete. The availability of the five key reference parameters (i.e.,  $\epsilon_{cu}$ ,  $f'_{cc}$ ,  $\epsilon_{c1}$ ,  $f'_{c1}$ , and  $\epsilon_{h,rupt}$ ) helps to model the whole curve of the FRP-confined concrete accurately, as was explained by Fallah Pour et al. [4]. An ANN can handle a complex database with large variables, identify sensitivity of input and output parameters, and establish relations between the input and output variables.

This study, as the first study in the literature, used an ANN technique to predict the transition zone on the stress–strain relationship and hoop rupture strain of FRP-confined concrete. The accuracy of the ultimate point prediction on the curve was also examined. A comprehensive database collected by this research group was used. Firstly, a brief introduction of the database and the principals of an ANN were provided. Afterward, the influence of an input variable in an ANN to predict different critical points on the curves was examined. A sensitivity analysis was performed for examining the influence of input variables on the accuracy of the final selected ANN option. This was accompanied by model validation using different statistical indicators. At the end, the accuracy of the developed models by ANN was compared to that of existing models.

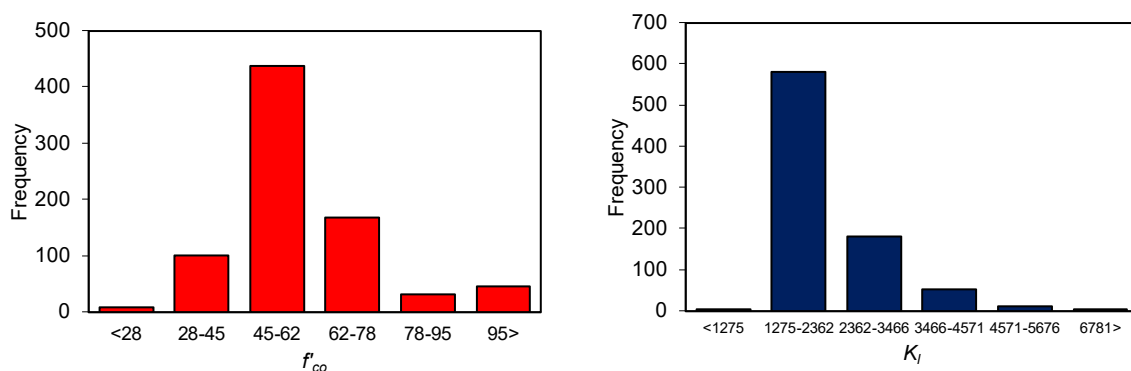
## 2. Experimental Test Database

The primary database used for this study for the ultimate condition can be found in [9,34], and the transition zone datasets can be found in [4] as the authors' previous studies. It should be noted that details of applied criteria to have a reliable and consistent primary database, leading to elimination of outlier datasets, can be found in [4]. The total data number for each key points is presented in Table 1. Figure 1 demonstrates the distribution of data.

**Table 1.** Summary of test results in the database.

Key Point	Number of Total Data	Number of Data after Evaluation
$f'_{cc}$	1063	836
$\epsilon_{cu}$	1063	571
$\epsilon_{h,rupt}$	506 *	443
$f'_{c1}$	260	260
$\epsilon_{c1}$	260	230

\* Only experimental  $\epsilon_{h,rupt}$  was considered in the calculation.



(a)

**Figure 1.** Cont.

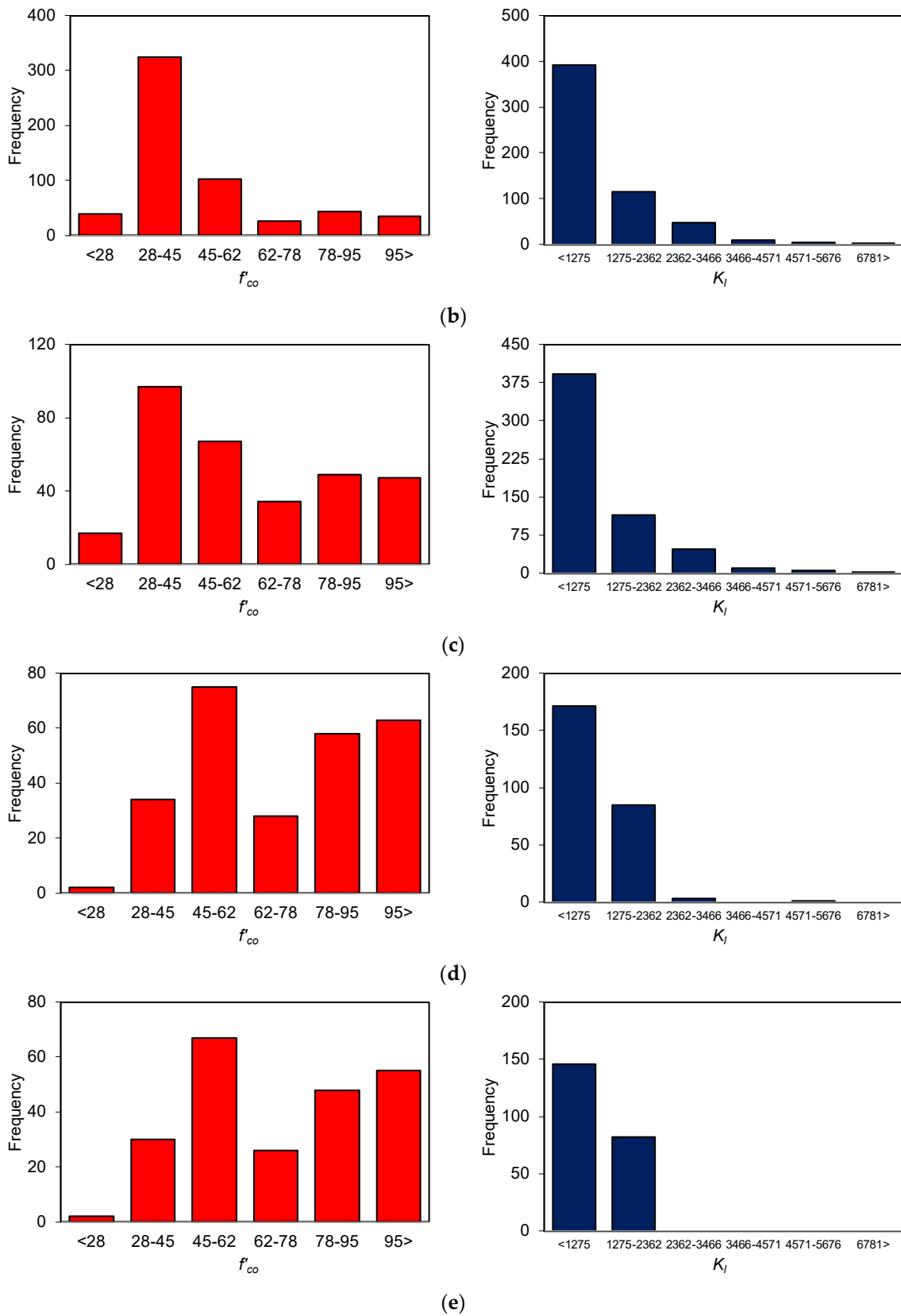


**Figure 1.** Frequency distribution of  $f'_{co}$  and  $K_I$  in prepared database for: (a)  $f'_{cc}$ , (b)  $\epsilon_{cu}$ , (c)  $\epsilon_{h,rup}$ , (d)  $f'_{c1}$ , and (e)  $\epsilon_{c1}$ .

### 3. Brief Overview of an Artificial Neural Network (ANN)

An artificial neural network (ANN) is a powerful instrument in regression analysis and classification of data [35]. A multilayer feed forward perceptron neural network based on an error back-propagation was used in this study. Based on Figure 2, ANN includes at least three layers. With more than three layers, they can be divided to three types of layers. These layers type include input, output, and hidden layer. In this method, the input vector is weighted ( $w_i$ ), and a bias ( $b$ ) is added to this value for each neuron, as shown in Equation (1).

$$y_i = \sum_{j=1}^m w_{ij}x_j + b_i \tag{1}$$

where  $x_1, x_2, \dots, x_m$  are input vectors,  $w_{i1}, w_{i2}, \dots, w_{im}$  are the weight of neuron  $I$ , and  $b_i$  is bias.

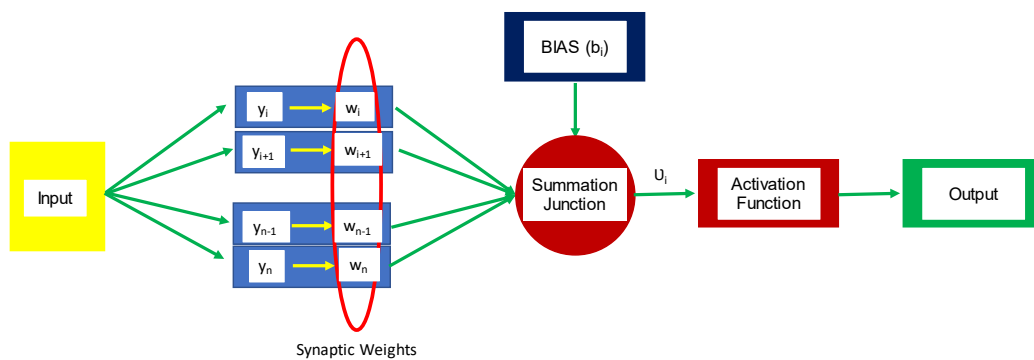


Figure 2. Nonlinear model of a neuron.

For describing a nonlinear relationship of input and output data, a nonlinear process on  $y_i$  is needed. This nonlinear process is called transfer (activation) function and is shown in Equation (2).

$$z_i = \varphi(y_i), \tag{2}$$

The selection of an appropriate transfer function for training the network is one of the influential parameters on the training procedure [36]. In this study, different transfer functions were used to achieve a highly accurate prediction model. The used transfer functions were Elliot sigmoid, logarithmic sigmoid, and linear and symmetric sigmoid transfer function.

Feed forward networks have an adaptive learning ability because of the adjustability of the neuron’s connection weights. The adjustment of the weight is known as knowledge storing. This indicates the need for comprehensive training to obtain an appropriate connection weight [37]. It should be noted that the applied algorithm in this study was a supervised algorithm, which needs both input–output pairs to perform network training. Equations (3) and (4) summarize the training procedure of networks:

$$g_t = \nabla f(t), \tag{3}$$

$$w_{j+1} = w_j - ag_t, \tag{4}$$

where  $w$  is the vector of weight,  $f$  is the objective function,  $g$  is the error gradient, and  $a$  is the learning rate. The iteration loop with all training datasets is referred to as an epoch, and training procedures sometimes need a couple of epochs to respect the considered criteria for stopping the iteration [38].

## 4. Optimal ANN Selection

### 4.1. Configuration of a Neural Network

It is well established that an increase in hidden layers and neuron numbers causes an increasing predictability of models. However, there is not an explicit design formula yet to determine the number of layers or neurons in an ANN analysis [16]. Additionally, using very complicated and strong modeling capability in an ANN architecture and small datasets leads to overfitting [39]. Although few hyper-parameter optimization algorithms, such as random research, existed [40], an experimental model tuning method was used in this study to find out the ANN architecture parameters, such as number of hidden layers and neurons. It should be mentioned that the experimental tuning was used for all investigated output parameters in this study. This indicates the existence of different architectural ANN maps for the investigated parameters.

### 4.2. Training of Network

MATLAB software was utilized to perform the ANN analysis. All combinations of input variables were trained utilizing Levenberg–Marquardt, Bayesian regularization, and scaled conjugate gradient algorithms [41]. Mean average error (MAE) was selected as the objective function. The dataset allocation, namely training and test, was similar for all analysis where the training datasets consisted of 70% of the total database, 15% as validation, and 15% as test datasets. The division was made by random selection for all three sets of divisions. In this study, the learning rate (LR) was determined by an experimental study, and it was decided to be 0.001 in the case of Levenberg–Marquardt and 0.005 for Bayesian regularization and scaled conjugate gradient algorithm. Additionally, the performance goal was set equal to  $1 \times 10^{-10}$ , and infinitive time was fixed for maximum time for the training procedure. At the end, min-max normalization methods were used for all the ANN analyses.

### 4.3. ANN Network

Initially, the best composition of input variables was selected. To choose the most accurate input combination, all combinations were evaluated using one hidden layer with various numbers of neurons ranging 10 to 30. This indicates the existence of three layers, namely input, hidden, and output. All parameters, e.g., goal performance, learning rate, and data division, were evaluated experimentally. Then, they were kept constant in this step of the study. The results indicated that the best LR was 0.005 for all the training functions. At this step, the symmetrical transfer function (tansig) was picked up for all analyses, but all three training functions of Levenberg–Marquardt, Bayesian regularization, and scaled conjugate gradient were analyzed. By determination of the best combination of input variables in the first step of the study, other parameters in the ANN architecture, including hidden layers and neuron numbers, transfer function variation, and learning rate, were investigated again. It should be noted that multiple transfer functions were examined, including logarithmic sigmoid transfer function (logsig), symmetric sigmoid transfer function (tansig), and linear transfer function (purelin).

### 4.4. Predictability Analysis

To evaluate the performance of the analysis in this study, different statistical indicators were considered. These indicators were MAE ( $AE = \frac{1}{n} \sum_{i=1}^n |\text{Mod}_i - \text{Exp}_i|$ ), average absolute error ( $AAE = \frac{\sum_{i=1}^N \left| \frac{\text{Mod}_i - \text{Exp}_i}{\text{Exp}_i} \right|}{N}$ ), mean ( $M = \frac{\sum_{i=1}^N \text{Mod}_i}{N}$ ), and root mean square error ( $RSME = \sqrt{\frac{\sum_{i=1}^N (\text{Mod}_i - \text{Exp}_i)^2}{N}}$  or  $MSE = \frac{\sum_{i=1}^N (\text{Mod}_i - \text{Exp}_i)^2}{N}$ ), where  $\text{Mod}_i$  and  $\text{Exp}_i$  are predicted and experimental values, respectively. MAE and AAE exhibit the accuracy of the model overall, M determines if the model exhibits overestimation or underestimation, and RMSE is an indicator of high errors.

### 5. ANN-Based Prediction Models

Figure 3 presents the flow chart of this study to predict the properties of FRP-confined concrete.

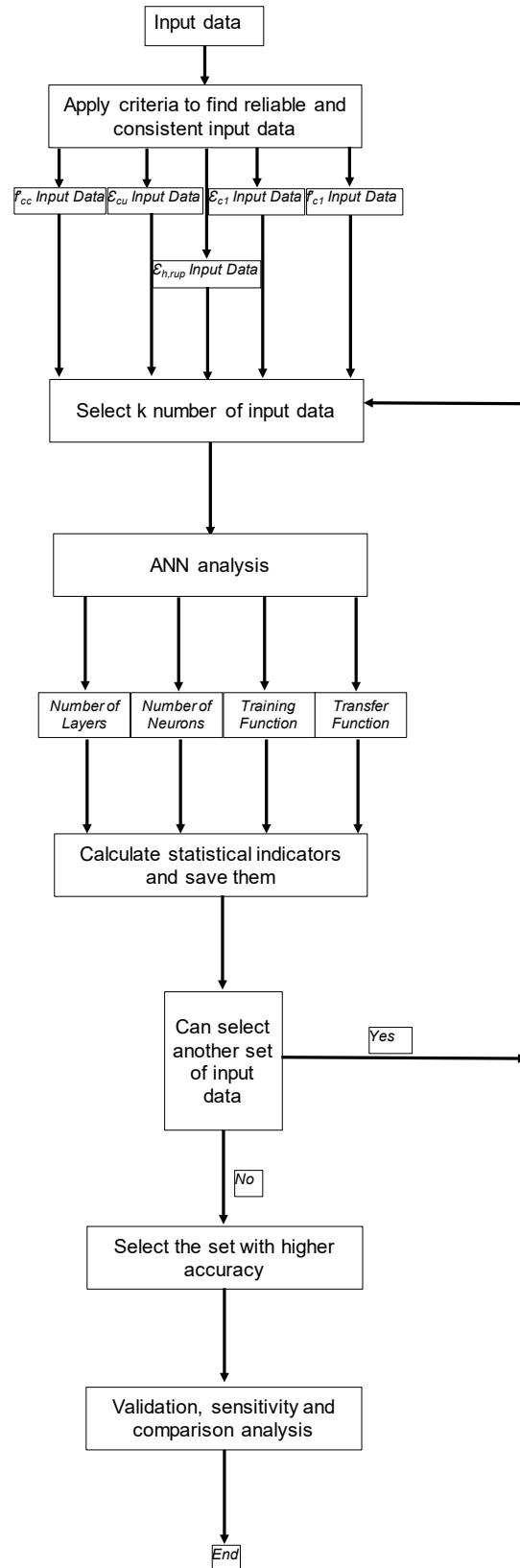


Figure 3. Flow chart of this study.

5.1. Ultimate Condition

Ultimate point is a significant point of the axial stress–strain relationship and exhibits  $\epsilon_{cu}$ ,  $f'_{cc}$ , and  $\epsilon_{h,rup}$ . Determination of this point offers a potential instrument to designers for predicting the maximum resistance of the system [42]. It should be noted that the corresponding strain to unconfined concrete strength ( $f'_{co}$ ), i.e.,  $\epsilon_{co}$ , has been considered as an input variable and was calculated by the proposed expression by Ref. [10] (i.e.,  $\epsilon_{co} = \frac{f'_{co}{}^{0.225}}{1000} \left(\frac{152}{D}\right)^{0.1} \left(\frac{2D}{H}\right)^{0.13}$ , where  $D$  and  $H$  are diameter and height of the specimen). This lowered the dependency of the input variables to experimental values and made the input variables readily available. This was the main purpose of this study to develop an accurate model, which uses readily available input data with simplicity to apply.

5.1.1.  $f'_{cc}$

To obtain the best combination of input variables, different variable sets were used to predict  $f'_{cc}$ . This was accompanied with the investigation of the correlation between input variables to avoid multicollinearity.

Table 2 shows the obtained Pearson’s correlation coefficients for all input variables and output data for ultimate condition. Based on the table, the highest correlation was for  $f'_{co}$  and  $\epsilon_{co}$ . As  $\epsilon_{co}$  is a function of  $f'_{co}$ , only  $f'_{co}$  was used to predict  $f'_{cc}$  in this study.

Table 2. Pearson’s correlation between input variables for ultimate condition.

	$E_f$	$t_f$	$D$	$f_f$	$\epsilon_{co}$	$f'_{co}$	$K_l$	$K_l/f'_{co}$	$\epsilon_{fu}$
$f'_{cc}$									
$E_f$	1.0								
$t_f$	−0.486	1.0							
$D$	−0.081	0.266	1.0						
$f_f$	0.780	−0.619	−0.122	1.0					
$\epsilon_{co}$	0.082	0.045	−0.213	0.010	1.0				
$f'_{co}$	0.081	0.045	−0.202	0.016	0.995	1.0			
$K_l$	0.276	0.230	−0.123	0.082	0.388	0.398	1.0		
$K_l/f'_{co}$	0.265	0.221	0.002	0.110	−0.207	−0.194	0.747	1.0	
$\epsilon_{fu}$	−0.531	0.010	−0.031	−0.106	−0.130	−0.124	−0.357	−0.303	1.0
$\epsilon_{cu}$									
$E_f$	1.0								
$t_f$	−0.431	1.0							
$D$	−0.137	0.368	1.0						
$f_f$	0.709	−0.594	−0.238	1.0					
$\epsilon_{co}$	0.153	−0.085	−0.428	0.163	1.0				
$f'_{co}$	0.122	−0.007	−0.228	0.092	0.945	1.0			
$K_l$	0.342	0.169	−0.134	0.175	0.378	0.365	1.0		
$K_l/f'_{co}$	0.319	0.208	0.026	0.148	−0.143	−0.158	0.781	1.0	
$\epsilon_{fu}$	−0.613	0.032	−0.027	−0.170	−0.132	−0.153	−0.364	−0.324	1.0
$\epsilon_{h,rup}$									
$E_f$	1.0								
$t_f$	−0.418	1.0							
$D$	−0.010	0.103	1.0						
$f_f$	0.655	−0.594	−0.135	1.0					
$\epsilon_{co}$	0.041	0.007	−0.361	0.053	1.0				
$f'_{co}$	0.023	0.055	−0.160	0.001	0.965	1.0			
$K_l$	0.344	0.165	−0.167	0.129	0.338	0.324	1.0		
$K_l/f'_{co}$	0.342	0.161	−0.089	0.151	−0.206	−0.224	0.772	1.0	
$\epsilon_{fu}$	−0.650	0.049	−0.084	−0.177	−0.046	−0.053	−0.375	−0.345	1.0

Table 3 shows the change in ANN performance of  $f'_{cc}$  for various sets of input variables. As shown, the Levenberg–Marquardt and Bayesian regularization algorithms showed the lowest AAE compared to the scaled conjugate gradient. Moreover, the hidden layer with 25 or 30 neurons generally developed the lowest AAE value, although some exceptions can be observed, especially for the Levenberg–Marquardt algorithm. It is also observed that the Bayesian regularization algorithm had the lowest AAE and RMSE among all the studied cases, and the accuracy of the prediction by this algorithm increased by increasing the input variables number. Additionally, a third set of input variables offered lower values of AAE compared to other analyzed sets. As a result, the third set of variables was selected as best combination of variables.

**Table 3.** Summary of different studied cases for input variables for  $f'_{cc}$ .

Input Variables	Levenberg–Marquardt														
	10 Neurons			15 Neurons			20 Neurons			25 Neurons			30 Neurons		
	AAE (%)	M (%)	RMSE (MPa)	AAE (%)	M (%)	RMSE (MPa)	AAE (%)	M (%)	RMSE (MPa)	AAE (%)	M (%)	RMSE (MPa)	AAE (%)	M (%)	RMSE (MPa)
$f'_{co}, K_l, \varepsilon_{fu}$	11.7	102.0	12.9	10.6	100.0	11.6	10.3	101.1	11.3	10.0	101.1	12.8	9.8	101.7	15.9
$f'_{co}, K_l, \varepsilon_{fu}, K_l/f'_{co}$	10.8	101.7	11.3	10.6	101.4	11.3	12.0	104.7	12.3	10.7	101.1	11.9	10.1	101.4	10.6
$f'_{co}, K_l, \varepsilon_{fu}, K_l/f'_{co}, E_{f_j}, f_j, t_f$	12.6	103.2	12.4	16.1	105.6	16.0	10.7	97.5	11.3	9.1	100.8	8.8	10.8	100.8	9.9
$f'_{co}, K_l, \varepsilon_{fu}, K_l/f'_{co}, E_{f_j}, f_j, t_f, D$	13.5	106.2	12.6	10.8	103.0	11.2	9.0	101.0	10.5	9.9	102.7	10.2	8.7	100.7	9.3
Input Variables	Bayesian Regularization														
	10 Neurons			15 Neurons			20 Neurons			25 Neurons			30 Neurons		
	AAE (%)	M (%)	RMSE (MPa)	AAE (%)	M (%)	RMSE (MPa)	AAE (%)	M (%)	RMSE (MPa)	AAE (%)	M (%)	RMSE (MPa)	AAE (%)	M (%)	RMSE (MPa)
$f'_{co}, K_l, \varepsilon_{fu}$	10.7	102.0	11.2	10.0	101.1	11.5	9.5	101.3	10.2	9.2	102.2	11.3	8.7	101.5	9.9
$f'_{co}, K_l, \varepsilon_{fu}, K_l/f'_{co}$	10.5	101.8	10.8	10.7	101.8	12.6	10.5	101.8	11.0	9.8	101.7	11.0	10.4	102.1	11.4
$f'_{co}, K_l, \varepsilon_{fu}, K_l/f'_{co}, E_{f_j}, f_j, t_f$	7.7	100.7	9.7	7.7	101.0	8.4	6.6	100.6	7.0	6.6	100.3	6.3	6.5	100.3	7.8
$f'_{co}, K_l, \varepsilon_{fu}, K_l/f'_{co}, E_{f_j}, f_j, t_f, D$	8.4	101.1	9.2	7.7	101.0	8.4	6.7	101.0	7.2	7.4	101.3	10.1	7.2	99.6	9.7
Input Variables	Scaled conjugate gradient														
	10 Neurons			15 Neurons			20 Neurons			25 Neurons			30 Neurons		
	AAE (%)	M (%)	RMSE (MPa)	AAE (%)	M (%)	RMSE (MPa)	AAE (%)	M (%)	RMSE (MPa)	AAE (%)	M (%)	RMSE (MPa)	AAE (%)	M (%)	RMSE (MPa)
$f'_{co}, K_l, \varepsilon_{fu}$	14.4	104.0	14.7	15.1	104.2	15.1	13.7	103.5	13.8	14.8	103.5	15.1	17.2	104.2	18.2
$f'_{co}, K_l, \varepsilon_{fu}, K_l/f'_{co}$	15.1	105.0	14.8	10.8	102.4	11.6	18.6	105.6	18.2	15.7	103.1	17.5	19.2	104.4	20.4
$f'_{co}, K_l, \varepsilon_{fu}, K_l/f'_{co}, E_{f_j}, f_j, t_f$	14.8	101.7	15.6	15.9	105.3	15.8	14.2	103.2	14.4	13.6	102.8	14.9	14.9	102.4	16.3
$f'_{co}, K_l, \varepsilon_{fu}, K_l/f'_{co}, E_{f_j}, f_j, t_f, D$	13.7	102.7	14.1	11.2	102.2	12.0	16.3	104.7	16.9	17.6	103.4	17.2	21.6	103.5	21.3

It should be noted that  $K_l/f'_{co}$ , as normalized lateral stiffness, was also considered as an input variable, although  $f'_{co}$  and  $K_l$  (lateral stiffness) existed in the input variables set. As can be seen in Table 2, the correlation coefficient for  $K_l$  and  $K_l/f'_{co}$  was 0.747.  $K_l/f'_{co}$  was

added to the variable set as an independent variable due to its significance in the mechanical characteristic of FRP-confined concrete. Equation (5) presents the best composition of input variables to obtain the highest accuracy for prediction of  $f'_{cc}$ .

$$f'_{cc} = f\left(f'_{co}, K_l, \frac{K_l}{f'_{co}}, \varepsilon_{fu}, E_f, t_f, f_f\right), \tag{5}$$

where  $t_f$  is the FRP total thickness,  $\varepsilon_{fu}$  is the fiber ultimate tensile strain,  $E_f$  is FRP elastic modulus, and  $f_f$  is fiber ultimate tensile strength.

As a second step, the influence of adding a second hidden layer and a number of neurons at each layer was investigated. It should be noted that using a higher number of hidden layers could increase the accuracy, but this would lead to more complicated models. Therefore, the hidden layers number was limited to two, and the variation of a neuron number in hidden layers was studied. Table 4 displays the influence of adding a second hidden layer to an ANN on  $f'_{cc}$  prediction. It should be noted that all the analyzed cases were not presented in this table due to the similarity of results. Furthermore, a scaled conjugate gradient algorithm was not studied in this step due its lower accuracy compared to the other algorithms. According to Table 4, two hidden layers with 15 neurons in first hidden layer and 10 neurons in second hidden layer using the Bayesian regularization algorithm developed the most accurate prediction for  $f'_{cc}$ . Comparing the most accurate model with one hidden layer (presented in Table 3) to that with two hidden layers (presented in Table 4) revealed that a more accurate prediction was obtained by two hidden layers; however, the accuracy improvement was not notably significant.

**Table 4.** Summary of different studied cases for different layers in predicting  $f'_{cc}$ .

	Levenberg–Marquardt			Bayesian Regularization		
	AAE (%)	M (%)	RMSE (MPa)	AAE (%)	M (%)	RMSE (MPa)
Two layers (4,5)	10.1	100.9	10.5	10.1	101.0	10.7
Two layers (5,4)	11.1	102.8	11.7	9.5	101.6	10.1
Two layers (6,8)	8.7	100.9	10.1	9.0	101.4	9.8
Two layers (8,6)	10.9	99.3	12.9	8.2	101.4	9.3
Two layers (8,9)	9.2	101.7	9.7	9.3	101.4	10.0
Two layers (9,8)	8.5	101.0	8.9	9.2	101.4	10.0
Two layers (8,10)	14.6	102.8	15.7	9.3	101.6	10.1
Two layers (10,8)	7.7	101.1	8.6	10.4	101.8	11.3
Two layers (10,15)	9.9	101.5	10.9	9.4	102.1	10.0
Two layers (15,10)	10.2	101.4	12.0	6.4	100.4	7.4
Two layers (15,20)	7.5	101.0	8.3	9.2	102.1	10.1
Two layers (20,15)	9.4	101.3	10.4	8.8	101.6	9.4
Two layers (20,25)	8.9	102.6	9.1	6.6	100.6	7.9
Two layers (25,20)	9.4	102.2	10.2	9.2	101.6	9.9

The influence of a transfer function on the accuracy of  $f'_{cc}$  prediction is shown in Table 5. Due to the highest accuracy obtained by the Bayesian regularization algorithm, the influence of the transfer function was examined using this algorithm. Various transfer functions, such as tansig, logsig, pureline, Elliot sigmoid (elliotsig), and triangular basis (tribas), were studied. It should be noted that various combinations of a transfer function were initially studied to find the highest accuracy for  $f'_{cc}$  prediction. However, only a few of them are displayed in Table 5 due to the similarity of results. According to the table, tansig was the transfer function developing the most accurate prediction for  $f'_{cc}$ . Table 6 displays the final ANN parameters for  $f'_{cc}$  model.

**Table 5.** Summary of different studied cases for transfer function in predicting  $f'_{cc}$ .

Transfer Function	AAE (%)	M (%)	RMSE (MPa)
tansig-tansig	6.4	100.4	7.4
logsig-logsig	8.4	101.2	9.9
logsig-tansig	10.2	105.0	11.2
pureline-pureline	14.0	103.8	14.1
tansig-pureline	8.5	101.1	9.1
elliotsig-elliotsig	9.9	101.8	10.8
tribas-tribas	20.1	105.8	22.9
purelin-logsig	11.2	105.0	12.2

**Table 6.** Final ANN parameters for prediction models.

Parameter	Number of Hidden Layers	Number of Beurons First	Number of Beurons Second	Training Function	Transfer Function	Learning Rate	Objective Function
$f'_{cc}$	2	15	10	Bayesian regularization	tansig	0.005	MSE
$\epsilon_{cu}$	2	6	8	Levenberg–Marquardt	tansig	0.001	MSE
$\epsilon_{h,rip}$	2	10	15	Bayesian regularization	tansig	0.005	MSE
$f'_{c1}$	1	25	-	Bayesian regularization	tansig	0.005	MSE
$\epsilon_{c1}$	2	25	20	Levenberg–Marquardt	tansig	0.001	MSE

The developed model performance in predicting  $f'_{cc}$  is illustrated in Figure 4. According to Figure 4a, experimental and predicted  $f'_{cc}$  had a close consistency. In this figure, a 45° line was added, which is a representative of the perfect agreement. Based on Figure 4b, the best match with the imposed goal for accuracy (MSE) was observed at epoch's number 833. K-fold cross-validation was applied on the final ANN model for prediction of  $f'_{cc}$ . This analysis was performed to assess the machine learning performance on unseen data. In this analysis, the database was randomly split in a K division. The popular value for K ranges was 5 to 10. One of the K portions of the database was considered as a test dataset, and all remaining K-1 portions were considered as a training dataset. The ANN analysis was performed and the obtained statistical indicators, which showed the model performance, were kept. This procedure was repeated for K times, and a comparison between the obtained statistical indicators was made. By this procedure, each individual dataset could be used at least one time as a test dataset, and K-1 time as a training dataset. It should be noted that, in this study, AAE was used to compare the performance of the models using various training and test datasets, i.e., K-fold cross-validation. Figure 4c illustrates the obtained AAE by K-fold cross-validation. In this figure, lower limit, upper limit, and average of the obtained AAE were shown. Maximum AAE was obtained at 10.2%, and the minimum value was obtained at 6.4%. This indicates that dataset selection caused a variation of accuracy in the developed model.

### 5.1.2. $\epsilon_{cu}$

A similar procedure to that used for  $f'_{cc}$  was performed to find the best ANN architecture for predicting  $\epsilon_{cu}$ . The obtained outcome for independent variables variations and the number of layers is presented in Table 7. Based on the table, the combination of variables with the Bayesian regularization algorithm offered the highest accuracy compared to the other algorithms. Equation (6) presents the best composition of input variables to obtain the highest accuracy for the prediction of  $\epsilon_{cu}$ .

$$\epsilon_{cu} = f \left( f'_{co}, \frac{K_1}{f'_{co}}, \epsilon_{fu}, k_2, E_f, t_f, f_f, \epsilon_{co}, D \right), \tag{6}$$

where  $k_2$  is strain enhancement coefficient proposed by Fallah Pour et al. [4]. As shown in Table 2, simultaneous use of  $f'_{co}$  and  $\epsilon_{co}$  could lead to multicollinearity in  $\epsilon_{cu}$  model. However, the obtained results of  $\epsilon_{cu}$  showed that using both parameters in predicting the model resulted in a more accurate prediction.

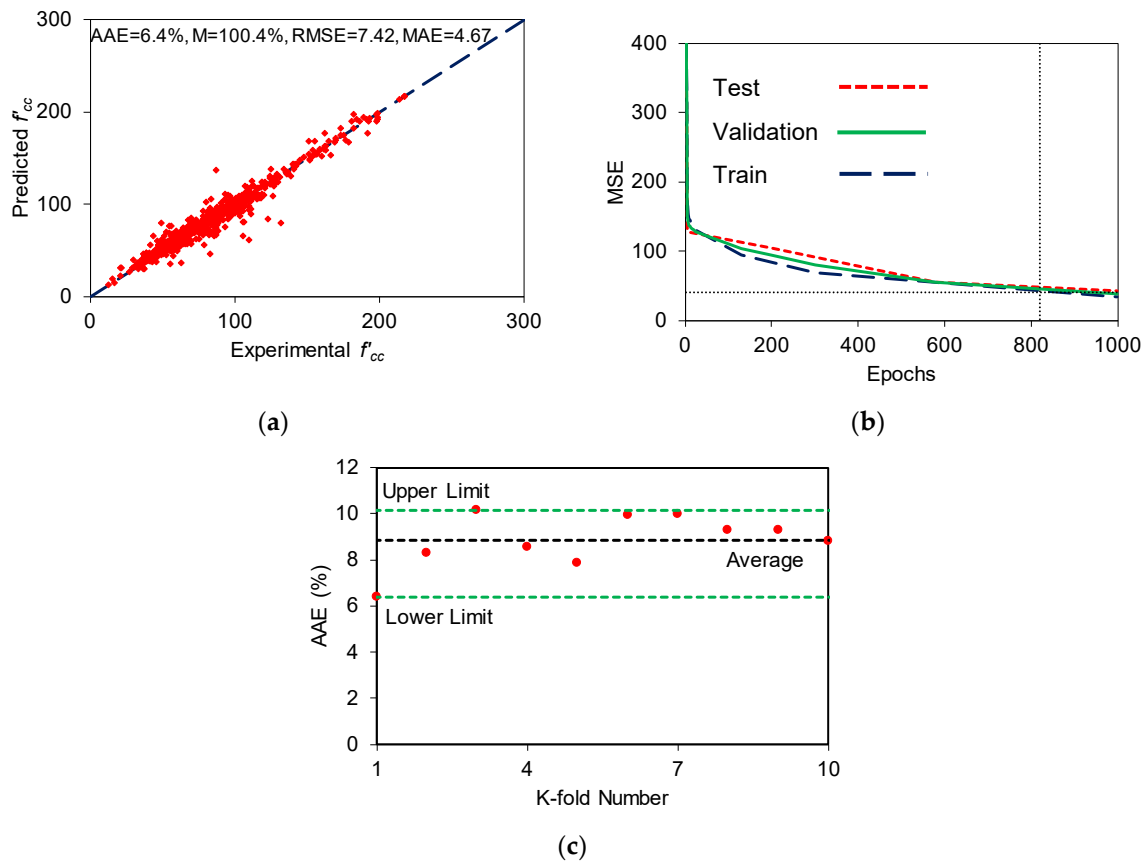


**Figure 4.** Performance of a developed model for compressive strength ( $f'_{cc}$ ): (a) Comparison of model prediction and experimental values, (b) performance accuracy, and (c) cross-validation analysis.

**Table 7.** Summary of different studied cases for input variables for  $\epsilon_{cu}$ .

Input Variables	Levenberg–Marquardt														
	10 Neurons			15 Neurons			20 Neurons			25 Neurons			30 Neurons		
	AAE (%)	M (%)	RMSE (%)	AAE (%)	M (%)	RMSE (%)	AAE (%)	M (%)	RMSE (%)	AAE (%)	M (%)	RMSE (%)	AAE (%)	M (%)	RMSE (%)
$f'_{co}, K_1/f'_{co}, \epsilon_{fu}$	32.6	96.3	0.005	31.8	99.3	0.005	31.3	101.1	0.005	35.0	98.5	0.006	37.0	96.5	0.007
$f'_{co}, K_1/f'_{co}, \epsilon_{fu}, k_2$	35.2	102.2	0.006	30.5	101.1	0.006	31.0	103.1	0.005	30.7	99.9	0.005	39.4	113.3	0.007
$f'_{co}, K_1/f'_{co}, \epsilon_{fu}, k_2, E_f$	32.3	100.4	0.005	29.4	98.0	0.005	28.6	102.0	0.005	37.4	86.7	0.006	25.8	100.1	0.005
$f'_{co}, K_1/f'_{co}, \epsilon_{fu}, k_2, E_f, t_f$	32.3	100.4	0.0055	32.6	101.0	0.005	25.6	101.8	0.005	40.2	90.1	0.006	25.6	101.8	0.005
$f'_{co}, K_1/f'_{co}, \epsilon_{fu}, k_2, E_f, t_f, f_f$	28.6	99.3	0.005	25.0	106.2	0.004	24.4	101.0	0.005	23.7	101.3	0.005	22.4	104.9	0.004
$f'_{co}, K_1/f'_{co}, \epsilon_{fu}, k_2, E_f, t_f, f_f, \epsilon_{co}, D$	31.4	64.5	0.006	24.5	102.9	0.004	22.4	103.4	0.004	20.1	109.1	0.004	20.9	56.3	0.004

Table 7. Cont.

Input Variables	Bayesian Regularization														
	10 Neurons			15 Neurons			20 Neurons			25 Neurons			30 Neurons		
	AAE (%)	M (%)	RMSE (%)	AAE (%)	M (%)	RMSE (%)	AAE (%)	M (%)	RMSE (%)	AAE (%)	M (%)	RMSE (%)	AAE (%)	M (%)	RMSE (%)
$f'_{co}, K_1/f'_{co}, \epsilon_{fu}$	30.6	100.5	0.005	29.3	101.8	0.005	34.0	100.0	0.006	30.5	99.1	0.005	29.5	97.1	0.006
$f'_{co}, K_1/f'_{co}, \epsilon_{fu}, k_2$	29.7	99.8	0.005	29.7	100.8	0.005	29.6	99.7	0.005	31.6	106.2	0.005	30.7	99.5	0.005
$f'_{co}, K_1/f'_{co}, \epsilon_{fu}, k_2, E_f$	26.5	101.2	0.005	28.5	103.2	0.005	21.4	103.2	0.004	19.9	102.7	0.004	19.0	100.2	0.004
$f'_{co}, K_1/f'_{co}, \epsilon_{fu}, k_2, E_f, t_f$	26.5	101.8	0.005	23.9	100.0	0.004	21.8	100.9	0.004	18.2	99.9	0.003	21.8	100.9	0.004
$f'_{co}, K_1/f'_{co}, \epsilon_{fu}, k_2, E_f, t_f, f_f$	22.9	102.1	0.004	21.2	115.0	0.004	18.2	100.9	0.004	16.9	100.3	0.003	21.4	84.9	0.004
$f'_{co}, K_1/f'_{co}, \epsilon_{fu}, k_2, E_f, t_f, f_f, \epsilon_{co}, D$	21.5	103.8	0.004	17.9	102.4	0.004	16.3	99.5	0.004	14.8	100.9	0.003	14.9	99.9	0.004
Input Variables	Scaled Conjugate Gradient														
	10 Neurons			15 Neurons			20 Neurons			25 Neurons			30 Neurons		
	AAE (%)	M (%)	RMSE (%)	AAE (%)	M (%)	RMSE (%)	AAE (%)	M (%)	RMSE (%)	AAE (%)	M (%)	RMSE (%)	AAE (%)	M (%)	RMSE (%)
$f'_{co}, K_1/f'_{co}, \epsilon_{fu}$	40.6	101.1	0.006	47.6	104.5	0.007	35.7	99.1	0.006	42.1	103.1	0.007	44.1	101.1	0.008
$f'_{co}, K_1/f'_{co}, \epsilon_{fu}, k_2$	42.0	98.7	0.007	40.2	100.4	0.006	44.8	100.6	0.007	36.7	105.0	0.006	35.4	99.7	0.006
$f'_{co}, K_1/f'_{co}, \epsilon_{fu}, k_2, E_f$	41.9	102.8	0.007	39.6	104.1	0.006	33.1	99.4	0.005	47.7	106.5	0.007	49.5	120.5	0.008
$f'_{co}, K_1/f'_{co}, \epsilon_{fu}, k_2, E_f, t_f$	48.6	127.3	0.007	40.9	100.0	0.007	35.4	97.5	0.006	41.2	107.0	0.007	35.4	97.5	0.006
$f'_{co}, K_1/f'_{co}, \epsilon_{fu}, k_2, E_f, t_f, f_f$	41.8	95.6	0.007	38.6	97.6	0.006	41.0	101.4	0.007	40.1	103.3	0.006	40.4	93.4	0.007
$f'_{co}, K_1/f'_{co}, \epsilon_{fu}, k_2, E_f, t_f, f_f, \epsilon_{co}, D$	39.1	112.6	0.007	42.9	102.0	0.006	34.4	107.5	0.006	36.1	103.2	0.006	36.7	96.1	0.006

ANN parameters, which offered more accurate model for predicting  $\epsilon_{cu}$ , are presented in Table 6. According to the table, the Levenberg–Marquardt algorithm and the tansig transfer function with two hidden layers of six and eight neurons offered the most accurate and simple ANN model for predicting  $\epsilon_{cu}$ . Cross-validation analysis was carried out on the final ANN map. The developed model performance for  $\epsilon_{cu}$  is shown in Figure 5. Based on Figure 5a, the predicted  $\epsilon_{cu}$  values were close to experimental  $\epsilon_{cu}$  values. Figure 5b exhibits that the considered goal as limit for BP neural network analysis of  $\epsilon_{cu}$  reached at epoch of 95. Additionally, it is shown in Figure 5c that, similar to  $f'_{cc}$ , the selection of the dataset exhibited a major influence on the  $\epsilon_{cu}$  model accuracy.

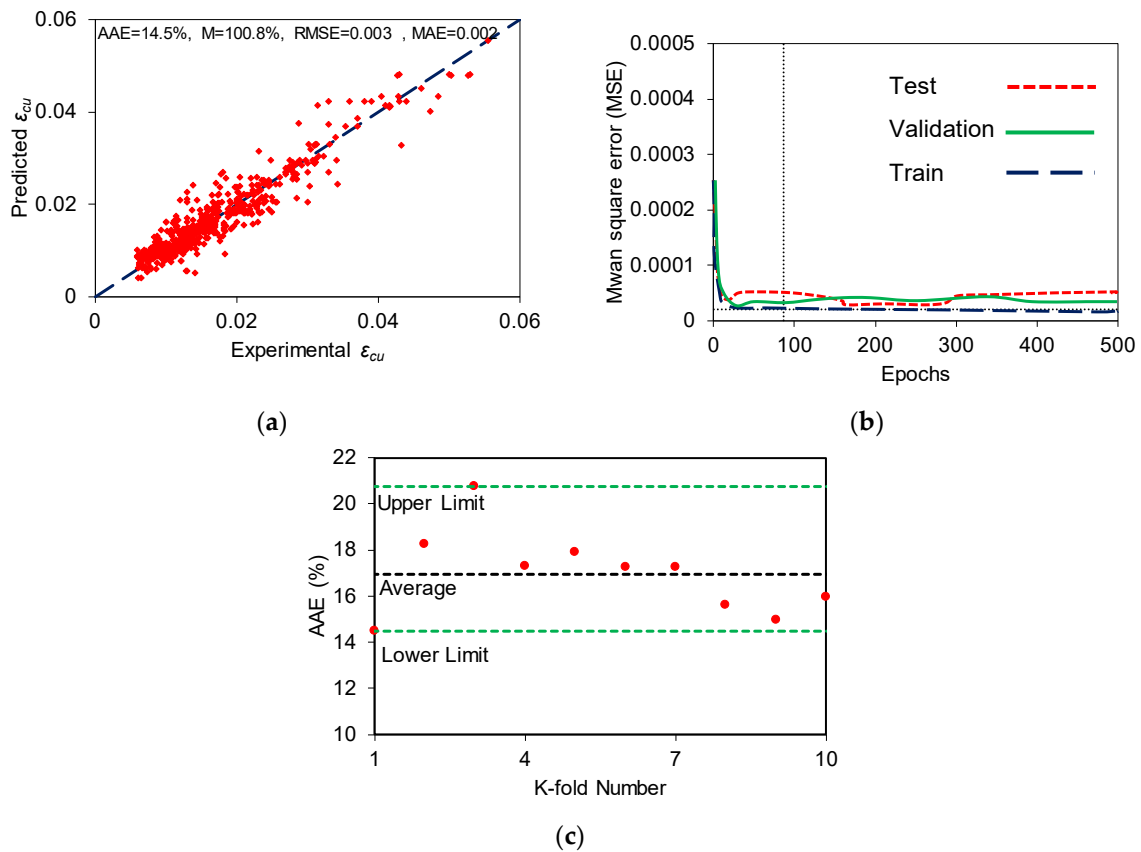


**Figure 5.** Performance of a developed model for ultimate axial strain ( $\epsilon_{cu}$ ): (a) Comparison of model prediction and experimental values, (b) performance accuracy, and (c) cross-validation analysis.

5.1.3.  $\epsilon_{h,rup}$

A similar procedure explained for  $f'_{cc}$  and  $\epsilon_{cu}$  was followed to determine the most accurate BP neural network model for  $\epsilon_{h,rup}$  prediction. Based on the obtained results, input variables presented in Equation (7) with the Bayesian regularization algorithm and 25 neurons developed the most accurate predictions of  $\epsilon_{h,rup}$ .

$$\epsilon_{h,rup} = f(f_{lco}, \epsilon_{co}, K_l, E_f, t_f, f_f, D, H), \tag{7}$$

According to Table 6, using two hidden layers having 10 and 15 neurons in each hidden layer offered the most accurate model. Similar to  $f'_{cc}$  and  $\epsilon_{cu}$ , applying tansig as the transfer function led to the development of the most accurate prediction of  $\epsilon_{h,rup}$  when compared to other transfer functions. Figure 6 exhibits the developed  $\epsilon_{h,rup}$  model performance. Based on Figure 6a, predicted  $\epsilon_{h,rup}$  had close values to experimental  $\epsilon_{h,rup}$  values. In Figure 6b, the best match between accuracy criteria for the ANN model and the least difference between train and validation datasets was at epoch of 395. Figure 6c displays that, similar to  $f'_{cc}$  and  $\epsilon_{cu}$ , the performance of the ANN depended significantly on the selection of different types of datasets, i.e., train, test, and validation.

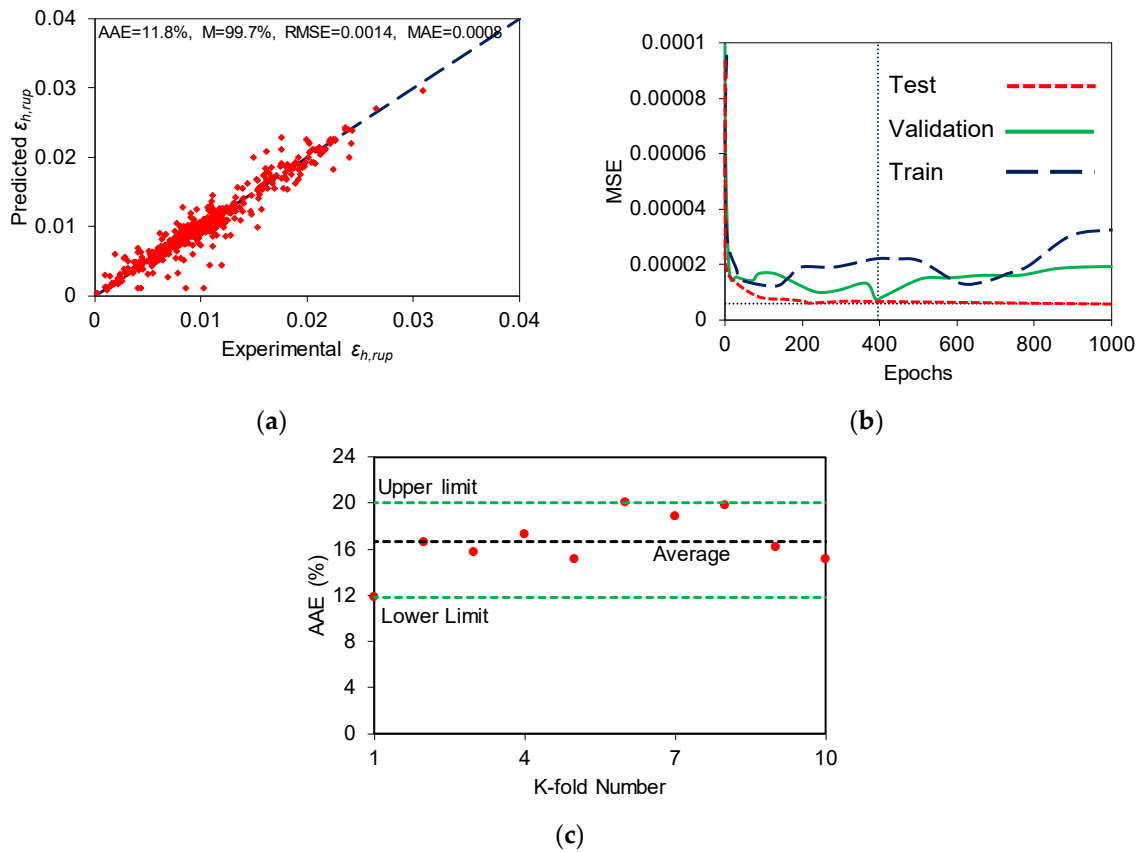


**Figure 6.** Performance of a developed model for hoop rupture strain ( $\epsilon_{h,rupt}$ ): (a) Comparison of model prediction and experimental values, (b) performance accuracy, and (c) cross-validation analysis.

5.2. Transition Zone

Transition zone ( $f'_{c1}, \epsilon_{c1}$ ) determines the point in which the first ascending nonlinear segment shifts toward the second ascending quasi-linear segment on the curve. As explained for the ultimate condition, using a similar database to the previous work of this research group offers an ability to compare the developed models with existing best performing models.

5.2.1.  $f'_{c1}$

Equation (8) presents the best composition of input variables for the prediction of  $f'_{c1}$  using an ANN analysis.

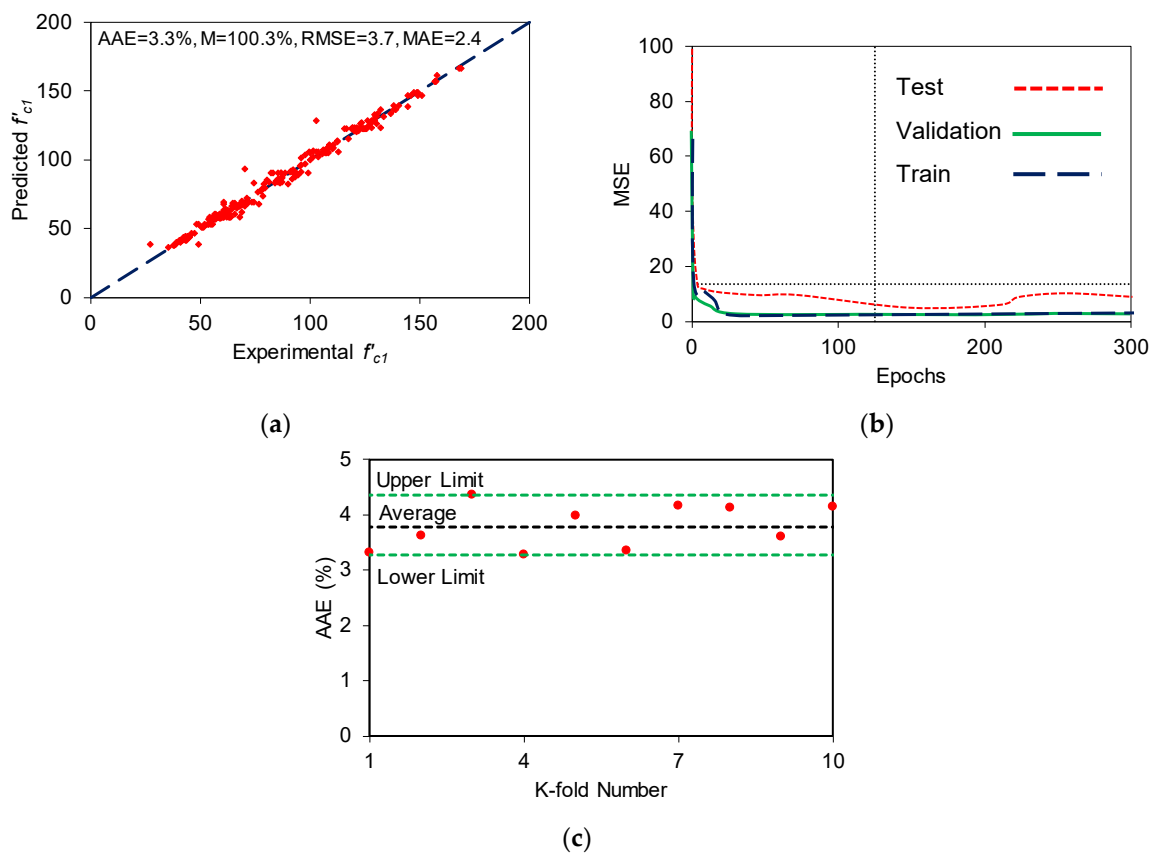
$$f'_{c1} = f\left(f'_{co}, K_l, \frac{K_l}{f'_{co}}, \epsilon_{fu}, E_f, t_f, f_f, D, H\right), \tag{8}$$

Table 8 exhibits the obtained Pearson’s correlation coefficients for all input variables and output data for a transition zone. As can be seen, similar to the ultimate condition,  $f'_{co}$  and  $\epsilon_{co}$  had maximum correlation, and the best prediction was obtained when only  $f'_{co}$  was considered. As shown in Table 6, one hidden layer having 25 neurons with the Bayesian regularization algorithm and tansig as a transfer function was considered as the final ANN prediction parameters for  $f'_{c1}$ . Although an increasing hidden layers number could cause increasing the  $f'_{c1}$  prediction accuracy, the improvement of the accuracy was not significant.

The performance of the developed model for  $f'_{c1}$  is illustrated in Figure 7. Figure 7a exhibits that the values recorded by experiments and model predictions had a good agreement. Figure 7b illustrates that the accuracy goal in  $f'_{c1}$  analysis was met at epoch of 136. Figure 7c illustrates the K-fold cross-validation for  $f'_{c1}$  prediction. As can be seen, the variation of test datasets did not significantly influence the accuracy of the  $f'_{c1}$  model.

**Table 8.** Pearson’s correlation between input variables for the transition zone.

	$E_f$	$t_f$	$D$	$f_f$	$\varepsilon_{co}$	$f'_{co}$	$K_l$	$K_l/f'_{co}$	$\varepsilon_{fu}$
	$f'_{c1}$								
$E_f$	1.0								
$t_f$	-0.453	1.0							
$D$	0.047	0.230	1.0						
$f_f$	0.314	-0.431	0.021	1.0					
$\varepsilon_{co}$	-0.234	0.548	-0.332	-0.166	1.0				
$f'_{co}$	-0.291	0.712	-0.054	-0.242	0.888	1.0			
$K_l$	0.401	0.455	-0.057	0.024	0.471	0.471	1.0		
$K_l/f'_{co}$	0.648	-0.066	0.003	0.149	-0.275	-0.281	0.594	1.0	
$\varepsilon_{fu}$	-0.909	0.556	0.009	-0.557	0.249	0.342	-0.307	-0.567	1.0
	$\varepsilon_{c1}$								
$E_f$	1.0								
$t_f$	-0.523	1.0							
$D$	0.063	0.197	1.0						
$f_f$	0.922	-0.435	0.116	1.0					
$\varepsilon_{co}$	-0.121	0.497	-0.374	-0.135	1.0				
$f'_{co}$	-0.218	0.679	-0.071	-0.208	0.872	1.0			
$K_l$	0.140	0.643	-0.056	0.197	0.618	0.622	1.0		
$K_l/f'_{co}$	0.372	0.197	-0.008	0.435	-0.039	-0.128	0.661	1.0	
$\varepsilon_{fu}$	-0.969	0.503	-0.030	-0.821	0.104	0.215	-0.144	-0.377	1.0



**Figure 7.** Performance of a developed model for axial strength at a transition point ( $f'_{c1}$ ): (a) Comparison of model prediction and experimental values, (b) performance accuracy, and (c) cross-validation analysis.

5.2.2.  $\epsilon_{c1}$

The most accurate model for predicting  $\epsilon_{c1}$  by variation of input data was obtained by using 30 neurons in one hidden layer and the Levenberg–Marquardt algorithm with the tansig transfer function. An in-depth investigation on the correlation between input variables was performed similar to the other prediction models, and the obtained result was similar to that of  $\epsilon_{cu}$  and  $\epsilon_{h,rup}$ . The obtained results revealed that the Pearson’s correlation for  $f'_{co}$  and  $\epsilon_{co}$  had the highest correlation coefficient, and only one of these input variables should be used to avoid multicollinearity, as illustrated in Table 8. However, the maximum accuracy was obtained when both  $f'_{co}$  and  $\epsilon_{co}$  were used. Equation (9) presents the input parameters, which offered the highest accuracy for  $\epsilon_{c1}$  prediction.

$$\epsilon_{c1} = f\left(f'_{co}, \frac{K_l}{f'_{co}}, K_l, E_f, t_f, f_f, \epsilon_{co}, D\right), \tag{9}$$

As displayed in Table 6, using two hidden layers with 25 and 20 neurons developed the most accurate predictions for  $\epsilon_{c1}$ . Furthermore, analysis of the transfer function showed that tansig offered the most accurate  $\epsilon_{c1}$ . The performance of the developed model for  $\epsilon_{c1}$  is shown in Figure 8. Based on Figure 8a, similar to other key reference points, the predicted values of  $\epsilon_{c1}$  were in good consistency with the recorded values in the experiments. Based on Figure 8b, the imposed criteria on MSE in the analysis was respected early in the calculation. Finally, as per Figure 8c, AAE varied significantly by the variation of test dataset of  $\epsilon_{c1}$ .

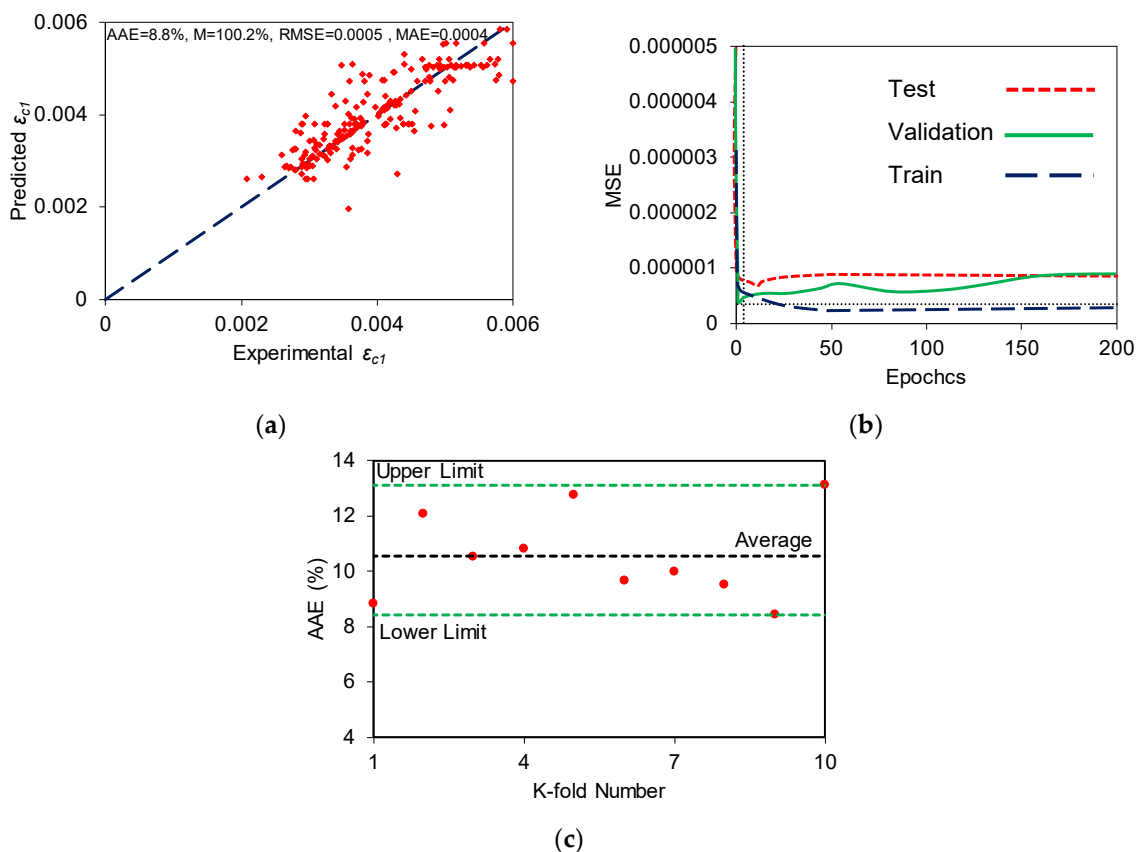


**Figure 8.** Performance of a developed model for axial strain at a transition point ( $\epsilon_{c1}$ ): (a) Comparison of model prediction and experimental values, (b) performance accuracy, and (c) cross-validation analysis.

### 6. Model Verification

#### 6.1. Sensitivity Analysis

For evaluating the impact of different independent input variables on developed prediction models, Equation (10) is used. This equation is used by various studies in data-driven methods (e.g., [43,44]).

$$r(Inp_{k,i}, \mu_k) = \frac{\sum_{i=1}^n (Inp_{k,i} - \overline{Inp_k})(\mu_i - \bar{\mu})}{\sqrt{\sum_{i=1}^n (Inp_{k,i} - \overline{Inp_k})^2 \sum_{i=1}^n (\mu_i - \bar{\mu})^2}} \tag{10}$$

where  $r$  is the relevance factor.  $Inp_{k,i}$  and  $\overline{Inp_k}$  are the  $i$ th of the  $k$ th and average of  $k$ th input variable, respectively.  $\mu_i$  is  $i$ th of the  $k$ th dependent variable, and  $\bar{\mu}$  is average of  $k$ th dependent variable. The results of sensitivity analysis for assessing the impact of each input on the ultimate condition predictions are observed in Figure 9. Based on Figure 9a,  $K_I$  and  $f'_{co}$  had highest impact on predicting  $f'_{cc}$ . Moreover, all the input variables exhibited a positive influence on  $f'_{cc}$ , except  $f_f$  and  $\epsilon_{fu}$ . Conversely,  $\epsilon_{cu}$  prediction was significantly influenced by  $\epsilon_{fu}$ , according to Figure 9b. Additionally,  $K_I/f'_{co}$ ,  $t_f$ , and  $k_2$  developed a positive influence, the same as  $\epsilon_{fu}$ , but other input variables showed a negative effect on  $\epsilon_{cu}$  prediction. It should be mentioned that  $D$  had a negative influence on the  $\epsilon_{cu}$  prediction. According to Figure 9c, the only parameter with a positive influence on  $\epsilon_{h,rup}$  prediction was  $t_f$ , which was physically expected. Other input data, including  $K_I$ ,  $E_f$ , and  $f'_{co}$ , showed a negative influence. Moreover, height and diameter slightly influenced  $\epsilon_{h,rup}$  prediction, and their influence was negative.

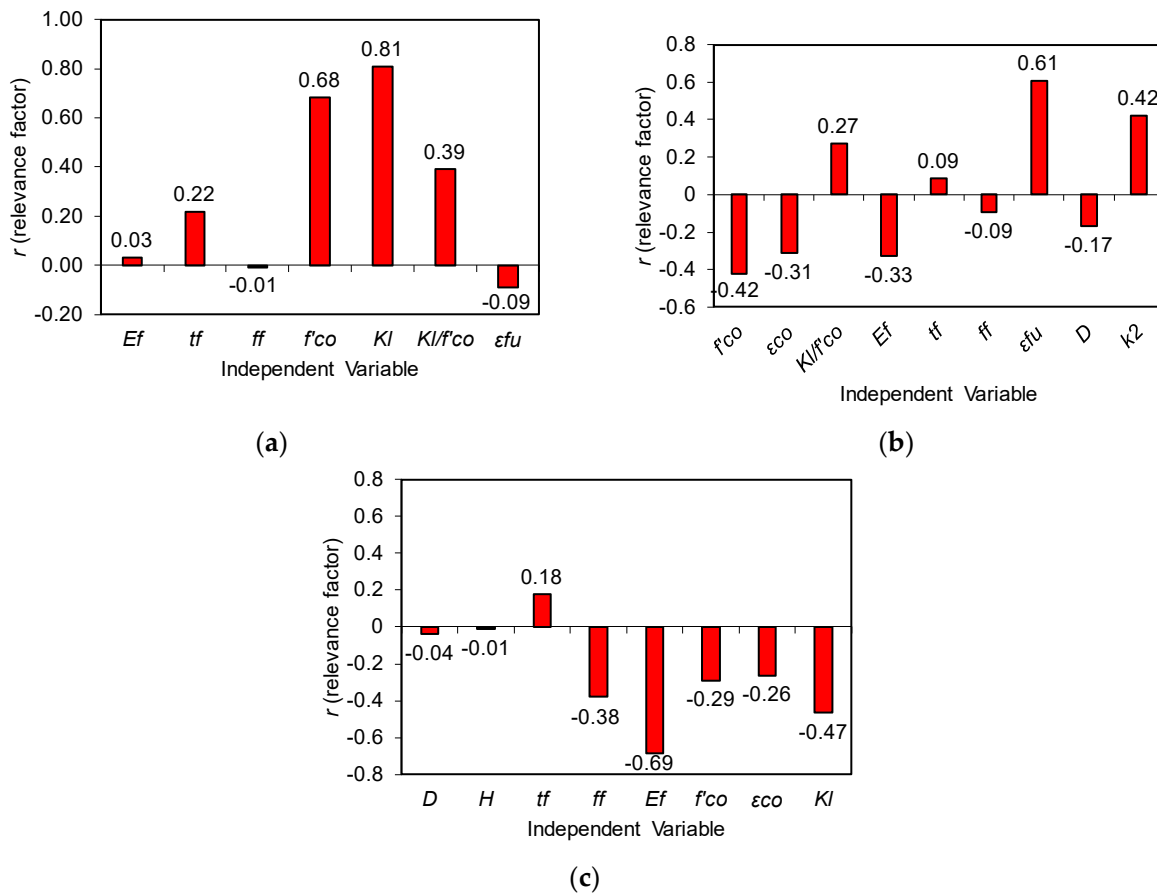


Figure 9. Obtained relevance factor for ultimate condition: (a)  $f'_{cc}$ , (b)  $\epsilon_{cu}$ , and (c)  $\epsilon_{h,rup}$ .

Figure 10 displays the influence of different input variables on the prediction of the transition zone of the stress–strain curve. According to Figure 10a, geometry parameters of concrete columns (i.e.,  $D$  and  $H$ ) slightly influenced the  $f'_{c1}$  prediction. Moreover,  $f'_{co}$ ,  $K_l$ , and  $t_f$  were the three parameters with the highest influence on  $f'_{c1}$  prediction, and their influences were positive. Additionally,  $E_f$ ,  $f_f$ , and  $K_l/f'_{co}$  negatively influenced the  $f'_{c1}$  prediction. According to Figure 10b, there were two input variables of  $E_f$  and  $f_f$ , which negatively influenced the prediction of  $\epsilon_{c1}$ , and other variables had a positive influence. It should be noted again that  $D$  as a geometry parameter slightly influenced  $\epsilon_{c1}$  prediction, similar to  $f'_{c1}$  and  $\epsilon_{h,rup}$  and opposite to  $\epsilon_{cu}$ .

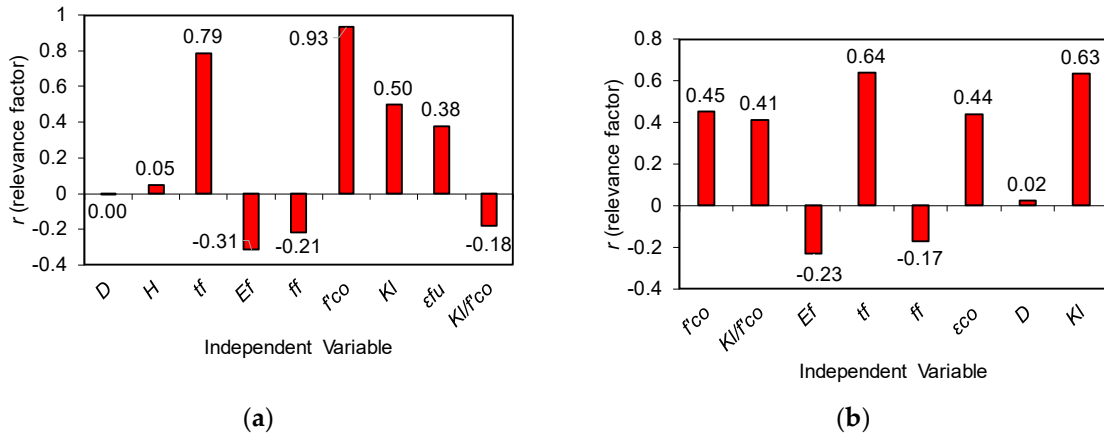


Figure 10. Obtained relevance factor for transition zone: (a)  $f'_{c1}$  and (b)  $\epsilon_{c1}$ .

### 6.2. Model Validation

Various statistical indicators were used in this study to verify the accuracy of the predictions. These indicators were RMSE, MAE,  $k$ ,  $k'$ , and  $R^2_0$ .  $k$  and  $k'$  are the regression slope through the origin, and  $R^2_0$  is the squared correlation coefficient.  $k$  is calculated by plotting experimental values against prediction values. Conversely,  $k'$  is the line slope by plotting prediction against experimental values. It should be noted that  $k$  and  $k'$  were used by Golbraikh and Tropsha [45], and  $R^2_0$  was introduced by Soleimani et al. [46]. Table 9 displays the statistical indicators used for predicted parameters of this study. It should be noted that the used thresholds of the statistical indicators were proposed in Refs. [46,47]. Based on the table, all the criteria were satisfied for all the predictions, except for  $\epsilon_{c1}$  where one of the criteria, i.e.,  $R_m$ , was not satisfied. Figure 11 shows the box plot of  $f'_{c1}$  and  $\epsilon_{c1}$  of this study. These parameters were selected as representative of the results. As can be seen in the figure, there were only a few samples where their predictions were in out-layers.

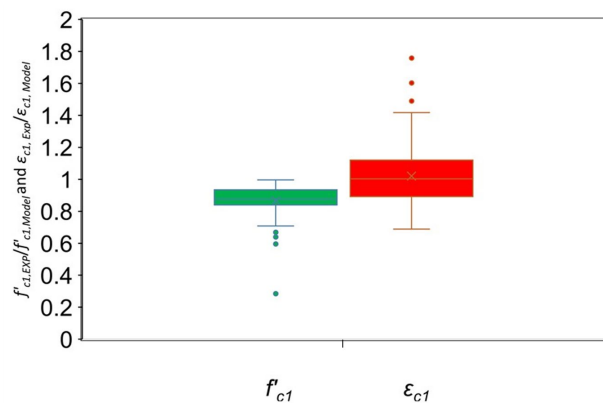


Figure 11. Box plot of  $f'_{c1}$  (left-hand side column) and  $\epsilon_{c1}$  (right-hand side column).

**Table 9.** Statistical indices for external validation of the developed models.

Index	Threshold	Transition Zone		Ultimate Condition		
		$f'_{c1}$	$\epsilon_{c1}$	$f'_{cc}$	$\epsilon_{cu}$	$\epsilon_{h.rup}$
$R = \frac{\sum_{i=1}^n (h_i - \bar{h}_i)(t_i - \bar{t}_i)}{\sqrt{\sum_{i=1}^n (h_i - \bar{h}_i)^2 \sum_{i=1}^n (t_i - \bar{t}_i)^2}}$	$R > 0.8$	0.99	0.84	0.98	0.94	0.96
$k = \frac{\sum_{i=1}^n (h_i t_i)}{\sum_{i=1}^n h_i^2}$	$0.85 < k < 1.15$	1.00	0.98	0.99	0.97	0.98
$k' = \frac{\sum_{i=1}^n (h_i t_i)}{\sum_{i=1}^n t_i^2}$	$0.85 < k' < 1.15$	0.99	1.02	1.01	1.03	1.02
$R_m = R^2 \left(1 - \sqrt{ R^2 - R_O^2 }\right)$	$R_m > 0.5$	0.87	0.33	0.76	0.60	0.67
$R_O^2 = 1 - \frac{\sum_{i=1}^n (t_i - h_i^O)^2}{\sum_{i=1}^n (t_i - \bar{t}_i)^2}$ $h_i^O = k t_i$	Should be close to 1	0.99	0.99	0.99	0.99	0.99
$R^2$	Should be close to 1	0.98	0.71	0.95	0.89	0.92
$RMSE = \sqrt{\frac{1}{n} \sum_{i=1}^n (h_i - t_i)^2}$	Should be minimum (based on output range)	3.47	0.0005	7.45	0.003	0.001
$MAE = \frac{1}{n} \sum_{i=1}^n  h_i - t_i $	Should be minimum (based on output range)	2.36	0.0003	4.67	0.002	0.001

### 7. Comparison of the Proposed and Existing Models

As explained previously, few studies used various types of a neural network method in predicting the ultimate point of FRP-confined concrete. These studies mostly used a neural network to predict  $f'_{cc}$ , and only two research studies focused on  $\epsilon_{cu}$ . In this section, developed predictions of the ultimate condition by an ANN were compared using  $R^2$ . The accuracy of the transition zone prediction was evaluated by comparing the proposed model with other design-oriented models.

#### 7.1. Ultimate Condition

Table 10 illustrates the comparison of  $f'_{cc}$  prediction by the developed model and that by existing ANN models (e.g., [48,49]). As can be seen, although a larger number of datasets was used in this study, the ANN model developed in this study offered a higher accuracy than the existing ANN models.

**Table 10.** Comparison between developed ANN models to predict  $f'_{cc}$ .

Model	Year	Number of Data	Prediction Parameter	$R^2$ -All
Naderpour et al. [25]	2010	213	$f'_{cc}$	0.89
Jiang et al. [16]	2020	169	$f'_{cc}$	0.98
Keshtegar et al. [48]	2021	780	$f'_{cc}/f'_{co}$	0.88
Cevik and Cabalar [23]	2008	110	$f'_{cc}$	0.97
Cevik [49]	2011	180	$f'_{cc}/f'_{co}$	0.94 *
Jalal and Ramezani-pour [24]	2012	128	$f'_{cc}$	0.95
Proposed model	-	836	$f'_{cc}$	0.99

\* The presented  $R^2$  is only for the test dataset.

A comparison between the accuracy of the existing ANN models and the ANN model developed in this study to predict  $\epsilon_{cu}$  is presented in Table 11. Based on the table, the proposed model offered a comparable accuracy while the number of analyzed datasets was largely compared to existing ANN models.

**Table 11.** Comparison between developed ANN models to predict  $\varepsilon_{cu}$ .

Model	Year	Number of Data	Prediction Parameter	R <sup>2</sup> -All
Jiang et al. [16]	2020	169	$\varepsilon_{cu}$	0.95
Keshtegar et al. [48]	2021	780	$\varepsilon_{cu} / \varepsilon_{co}$	0.86
Proposed model	-	836	$\varepsilon_{cu}$	0.89

As explained previously, using a similar database offers an efficient instrument to compare the obtained accuracy of the proposed models with available best performance models. Tables 12 and 13 present the accuracy of the proposed model and best performing models for estimating  $f'_{cc}$  (e.g., [50–55]) and  $\varepsilon_{cu}$  (e.g., [56–59]), respectively. Based on the tables, the model by Fallah Pour et al. [4] had the highest accuracy among existing models in predicting  $f'_{cc}$ . In addition, the model by Lim and Ozbakkaloglu [9] had the highest accuracy among existing models in predicting  $\varepsilon_{cu}$ . However, the proposed ANN models in this study had a higher accuracy than these best performing models in predicting  $f'_{cc}$  and  $\varepsilon_{cu}$ .

**Table 12.** Prediction statistics of the best performing  $f'_{cc}$  models.

Model	Test Data	AAE (%)	M (%)	SD (%)	RMSE (MPa)
Fallah Pour et al. [4]	836	12.3	100.0	16.3	14.9
Lim et al. [27]	836	12.7	105.0	17.1	15.2
Lim and Ozbakkaloglu [10]	836	12.9	102.9	16.8	14.6
Berthet et al. [50]	836	13.0	104.1	18.6	17.9
Wu and Zhou [51]	836	13.3	107.2	18.9	17.6
Pham and Hadi [33]	836	14.0	99.2	18.2	17.3
Al-Salloum [52]	836	14.1	108.7	21.0	22.0
Wei and Wu [53]	836	14.3	108.6	20.6	21.1
Wu and Wang [54]	836	14.3	108.6	20.6	21.1
Cevik [49]	836	20.2	107.0	30.1	19.8
Cevik et al. [55]	836	22.1	104.1	33.6	27.6
Proposed model	836	6.4	100.4	9.8	7.4

**Table 13.** Prediction statistics of the best performing  $\varepsilon_{cu}$  models.

Model	Test Data	AAE (%)	M (%)	SD (%)	RMSE (%)
Lim and Ozbakkaloglu [10]	571	20.1	97.5	23.9	0.50
Tamuzs et al. [56]	571	20.7	106.5	28.7	0.50
Fallah Pour et al. [4]	571	21.0	98.1	25.9	0.50
Teng et al. [57]	571	22.2	122.1	34.1	0.66
Lim et al. [27]	571	22.3	98.2	27.9	0.52
Binici [58]	571	22.6	124.1	37.7	0.85
Youssef et al. [8]	571	22.7	112.8	34.8	0.71
Berthet et al. [50]	571	23.2	121.5	41.9	0.75
Wei and Wu [53]	571	25.4	103.9	31.3	0.62
Pham and Hadi [33]	571	26.1	129.8	40.5	0.85
Miyauchi et al. [59]	571	27.4	122.1	40.9	0.65
Proposed model	571	14.5	100.8	20.2	0.30

## 7.2. Transition Zone

Tables 14 and 15 present the accuracy of the proposed model and best performing models to predict  $f'_{c1}$  and  $\varepsilon_{c1}$ . Based on these tables, the models by Fallah Pour et al. [4] had the highest accuracy among existing models in predicting  $f'_{c1}$  and  $\varepsilon_{c1}$ . However, the proposed ANN models in this study offered a higher accuracy than these best performing models in predicting the transition zone.

**Table 14.** Prediction statistics of the best performing  $f'_{c1}$  models.

Model	Test Data	AAE (%)	M (%)	SD (%)	RMSE (MPa)
Fallah Pour et al. [4]	256	8.5	98.0	9.8	8.5
Saafi at al. [6]	256	8.5	97.5	11.6	10.2
Lim and Ozbakkaloglu [10]	256	8.8	95.1	10.1	9.0
Youssef et al. [8]	256	9.2	96.7	12.8	11.5
Toutanji [7]	256	9.8	103	13.1	10.5
Proposed model	256	3.1	100.3	5.3	2.4

**Table 15.** Prediction statistics of the best performing  $\varepsilon_{c1}$  models.

Model	Test Data	AAE (%)	M (%)	SD (%)	RMSE (%)
Fallah Pour et al. [4]	228	14.7	98	18.6	0.08
Saafi at al. [6]	228	15	101	18.8	0.08
Toutanji [7]	228	15.6	103	19.3	0.08
Youssef et al. [8]	228	22.7	118	22.4	0.1
Proposed model	228	8.8	100.2	10.9	0.05

## 8. Conclusions

This study has presented the findings on the development of ANN models to predict transition and ultimate zones of FRP-confined concrete based on readily available parameters. Sensitivity analysis and model validation were used to verify the influence of the input parameters on the proposed models. It was shown that the accuracy of the ANN models for predicting ultimate condition was higher compared to that of the best performing existing models developed by different approaches. In addition, the ANN models proposed in this study offered a higher or similar accuracy compared to existing ANN models to predict the ultimate condition while a larger number of datasets was used in this study. Moreover, the developed ANN models used to predict the transition zone had significantly higher accuracy compared to best performing existing models. These observations indicate that the proposed ANN models captured the impact of the lateral confinement by FRP on the ultimate and transition zones of the confined concretes with a more robust performance compared to the existing models.

**Author Contributions:** Conceptualization, A.F.P. and A.G.; methodology, A.F.P. and A.G.; software, A.F.P.; validation, A.F.P. and A.G.; formal analysis, A.F.P. and A.G.; writing—original draft preparation, A.F.P.; writing—review and editing, A.G. All authors have read and agreed to the published version of the manuscript.

**Funding:** This research received no external funding.

**Institutional Review Board Statement:** Not applicable.

**Informed Consent Statement:** Not applicable.

**Data Availability Statement:** The data presented in this study are available on request from the corresponding author.

**Conflicts of Interest:** The authors declare no conflict of interest.

## Abbreviations

$E_f$	elastic modulus of fiber
$f_f$	ultimate tensile strength of fiber
$D$	diameter of FRP-confined concrete
$\varepsilon_f$	ultimate tensile strain of fiber
$f'_{co}$	compressive strength of unconfined concrete
$\varepsilon_{co}$	axial strain of unconfined concrete at $f'_{co}$
$t_f$	thickness of FRP tube
$K_l$	lateral stiffness
$K_l/f'_{co}$	normalized lateral stiffness
$f'_{cc}$	ultimate strength of FRP-confined concrete
$\varepsilon_{cu}$	ultimate strain of FRP-confined concrete
$\varepsilon_{h,rupt}$	strain of FRP tube at rupture
$f'_{c1}$	axial strength of FRP-confined concrete at transition zone
$\varepsilon_{c1}$	axial strain of FRP-confined concrete at transition zone

## References

- Ozbakkaloglu, T.; Lim, J.; Vincent, T. FRP-confined concrete in circular sections: Review and assessment of stress-strain models. *Eng. Struct.* **2013**, *49*, 1068–1088. [[CrossRef](#)]
- Pour, A.F.; Gholampour, A.; Ozbakkaloglu, T. Influence of the measurement method on axial strains of FRP-confined concrete under compression. *Compos. Struct.* **2018**, *188*, 415–424. [[CrossRef](#)]
- Pour, A.F.; Nguyen, G.; Vincent, T.; Ozbakkaloglu, T. Investigation of the compressive behavior and failure modes of unconfined and FRP-confined concrete using digital image correlation. *Compos. Struct.* **2020**, *252*, 112642. [[CrossRef](#)]
- Pour, A.F.; Ozbakkaloglu, T.; Vincent, T. Simplified design-oriented axial stress-strain model for FRP-confined normal- and high-strength concrete. *Eng. Struct.* **2018**, *175*, 501–516. [[CrossRef](#)]
- Lam, L.; Teng, J. Design-oriented stress–strain model for FRP-confined concrete. *Constr. Build. Mater.* **2003**, *17*, 471–489. [[CrossRef](#)]
- Saafi, M.; Toutanji, H.; Li, Z. Behavior of concrete columns confined with fiber reinforced polymer tubes. *Aci. Mater. J.* **1999**, *96*, 500–509.
- Toutanji, H. Stress-strain characteristics of concrete columns externally confined with advanced fiber composite sheets. *Aci. Mater. J.* **1999**, *96*, 397–404.
- Youssef, M.; Feng, M.; Mosallam, A.S. Stress–strain model for concrete confined by FRP composites. *Compos. Part B Eng.* **2007**, *38*, 614–628. [[CrossRef](#)]
- Lim, J.; Ozbakkaloglu, T. Confinement Model for FRP-Confined High-Strength Concrete. *J. Compos. Constr.* **2014**, *18*, 04013058. [[CrossRef](#)]
- Lim, J.; Ozbakkaloglu, T. Unified Stress-Strain Model for FRP and Actively Confined Normal-Strength and High-Strength Concrete. *J. Compos. Constr.* **2015**, *19*, 04014072. [[CrossRef](#)]
- Lim, J.; Ozbakkaloglu, T. Investigation of the Influence of the Application Path of Confining Pressure: Tests on Actively Confined and FRP-Confined Concretes. *J. Struct. Eng.* **2015**, *141*, 8. [[CrossRef](#)]
- Lim, J.; Ozbakkaloglu, T. Lateral Strain-to-Axial Strain Relationship of Confined Concrete. *J. Struct. Eng.* **2015**, *141*, 5. [[CrossRef](#)]
- Ozbakkaloglu, T.; Gholampour, A.; Lim, J. Damage-Plasticity Model for FRP-Confined Normal-Strength and High-Strength Concrete. *J. Compos. Constr.* **2016**, *20*, 6. [[CrossRef](#)]
- Bisby, L.; Sinclair, D.; Webster, M.; Stratford, T.W.; Take, W.A. Effects of Aspect Ratio on the Observed Hoop Strain Variation in FRP Confined Concrete Cylinders. In *Advanced Composites in Construction (ACIC) 2009 Conference Proceedings*; NetComposites Ltd.: Chesterfield, UK, 2009; pp. 570–581.
- Bisby, L.; Take, W.A.; Caspary, A. Quantifying strain variation FRP confined using digital image correlation: Proof-of-concept and initial results. In *Proceedings of the Asia–Pacific Conference on FRP in Structures*, Hong Kong, China, 12–14 December 2007.
- Jiang, K.; Han, Q.; Bai, Y.; Du, X. Data-driven ultimate conditions prediction and stress-strain model for FRP-confined concrete. *Compos. Struct.* **2020**, *242*, 112094. [[CrossRef](#)]
- Ghaboussi, J., Jr.; Garrett, J.; Wu, X. Knowledge-based modeling of material behavior with neural networks. *J. Eng. Mech.* **1991**, *117*, 132–153.
- Khan, K.; Iqbal, M.; Jalal, F.; Amin, M.N.; Alam, M.W.; Bardhan, A. Hybrid ANN models for durability of GFRP rebars in alkaline concrete environment using three swarm-based optimization algorithms. *Constr. Build. Mater.* **2022**, *352*, 128862. [[CrossRef](#)]
- Zheng, Z.; Tian, C.; Wei, X.; Zeng, C. Numerical investigation and ANN-based prediction on compressive strength and size effect using the concrete mesoscale concretization model. *Case Stud. Constr. Mater.* **2022**, *16*, e01056. [[CrossRef](#)]
- Huang, L.; Chen, J.; Tan, X. BP-ANN based bond strength prediction for FRP reinforced concrete at high temperature. *Eng. Struct.* **2022**, *257*, 114026. [[CrossRef](#)]

21. Benemaran, R.S.; Esmaeili-Falak, M.; Javadi, A. Predicting resilient modulus of flexible pavement foundation using extreme gradient boosting based optimised models. *Int. J. Pavement Eng.* **2022**, *9*, 1–20. [[CrossRef](#)]
22. Yildizel, S.; Toktas, A. ABC algorithm-based optimization and evaluation of nano carbon black added multi-layer microwave absorbing ultra weight foam concrete. *Mater. Today Commun.* **2022**, *32*, 104035. [[CrossRef](#)]
23. Cevik, A.; Cabalar, A. A genetic-programming-based formulation for the strength enhancement of fiber-reinforced-polymer-confined concrete cylinders. *J. Appl. Polym. Sci.* **2008**, *110*, 3087–3095. [[CrossRef](#)]
24. Jalal, M.; Ramezani-pour, A. Strength enhancement modeling of concrete cylinders confined with CFRP composites using artificial neural networks. *Compos. Part B Eng.* **2012**, *43*, 2990–3000. [[CrossRef](#)]
25. Naderpour, H.; Kheyroddin, A.; Amiri, G. Prediction of FRP-confined compressive strength of concrete using artificial neural networks. *Compos. Struct.* **2010**, *92*, 2817–2829. [[CrossRef](#)]
26. Yousif, D. New model of CFRP-confined circular columns: An approach. *Int. J. Civ. Eng. Technol.* **2013**, *4*, 98–110.
27. Lim, J.; Karakus, M.; Ozbakkaloglu, T. Evaluation of ultimate conditions of FRP-confined concrete columns using genetic programming. *Comput. Struct.* **2016**, *162*, 28–37. [[CrossRef](#)]
28. Wu, Y.-B.; Jin, G.-F.; Ding, T.; Meng, D. Modeling confinement efficiency of FRP-confined concrete column using radial basis function neural network. In Proceedings of the 2nd International Workshop on Intelligent Systems and Applications, Wuhan, China, 27 May 2010; IEEE: New York, NY, USA; pp. 1–6.
29. Cascardi, A.; Micelli, F.; Aiello, M.A. An Artificial Neural Networks model for the prediction of the compressive strength of FRP-confined concrete circular columns. *Eng. Struct.* **2017**, *140*, 199–208. [[CrossRef](#)]
30. Isleem, H.; Peng, F.; Tayeh, B. Confinement model for LRS FRP-confined concrete using conventional regression and artificial neural network techniques. *Compos. Struct.* **2022**, *279*, 114779. [[CrossRef](#)]
31. Alacali, S.; Akbaş, B.; Doran, B. Prediction of lateral confinement coefficient in reinforced concrete columns using neural network simulation. *Appl. Soft Comput.* **2011**, *11*, 2645–2655. [[CrossRef](#)]
32. Doran, B.; Yetilmezsoy, K.; Murtazaoglu, S. Application of fuzzy logic approach in predicting the lateral confinement coefficient for RC columns wrapped with CFRP. *Eng. Struct.* **2015**, *88*, 74–91. [[CrossRef](#)]
33. Pham, T.; Hadi, M. Predicting Stress and Strain of FRP-Confined Square/Rectangular Columns Using Artificial Neural Networks. *J. Compos. Constr.* **2014**, *18*, 6. [[CrossRef](#)]
34. Ozbakkaloglu, T.; Lim, J. Axial compressive behavior of FRP-confined concrete: Experimental test database and a new design-oriented model. *Compos. Part B Eng.* **2013**, *55*, 607–634. [[CrossRef](#)]
35. Haykin, S. *Neural Networks: A Comprehensive Foundation*; Pearson Education: North York, ON, Canada, 1999.
36. Baldo, N.; Manthos, E.; Miani, M. Stiffness modulus and marshall parameters of hot mix asphalts: Laboratory data modeling by artificial neural networks characterized by cross-validation. *Appl. Sci.* **2019**, *9*, 3502. [[CrossRef](#)]
37. Islam, M.; Dalhat, M.; Al Mamun, A. Road infrastructure investment limits based on minimal accidents using artificial neural network. *Appl. Sci.* **2022**, *12*, 11949. [[CrossRef](#)]
38. Khalaf, A.; Hanon, M. Prediction of Friction Coefficient for Ductile Cast Iron Using Artificial Neural Network Methodology Based on Experimental Investigation. *Appl. Sci.* **2022**, *12*, 11916. [[CrossRef](#)]
39. Ruder, S. An overview of gradient descent optimization algorithms. *arXiv* **2017**, arXiv:1609.04747v2.
40. Zhou, S.; Yang, C.; Su, Z.; Yu, P.; Jiao, J. An Aeromagnetic Compensation Algorithm Based on Radial Basis Function Artificial Neural Network. *Appl. Sci.* **2023**, *13*, 136. [[CrossRef](#)]
41. Goodfellow, I.; Bengio, Y.; Courville, A. *Deep Learning*; MIT Press: Cambridge, MA, USA, 2016.
42. Pour, A.F.; Faradonbeh, R.; Gholampour, A.; Ngo, T. Predicting ultimate condition and transition point on axial stress–strain curve of FRP-confined concrete using a meta-heuristic algorithm. *Compos. Struct.* **2023**, *304*, 116387. [[CrossRef](#)]
43. Chen, G.; Fu, K.; Liang, Z.; Sema, T.; Li, C.; Tontiwachwuthikul, P.; Idem, R. The genetic algorithm based back propagation neural network for MMP prediction in CO<sub>2</sub>-EOR process. *Fuel* **2014**, *126*, 202–212. [[CrossRef](#)]
44. Hosseinzadeh, M.; Hemmati-Sarapardeh, A. Toward a predictive model for estimating viscosity of ternary mixtures containing ionic liquids. *J. Mol. Liq.* **2014**, *200*, 340–348. [[CrossRef](#)]
45. Golbraikh, A.; Tropsha, A. Beware of q<sup>2</sup>! *J. Mol. Graph. Model.* **2002**, *20*, 269–276. [[CrossRef](#)]
46. Soleimani, S.; Rajaei, S.; Jiao, P.; Sabz, A.; Soheilinia, S. New prediction models for unconfined compressive strength of geopolymer stabilized soil using multi-genetic programming. *Measurement* **2018**, *113*, 99–107. [[CrossRef](#)]
47. Mohammadzadeh, S.; Bazaz, J.; Yazd, S.; Alavi, A. Deriving an intelligent model for soil compression index utilizing multi-genetic programming. *Env. Earth Sci.* **2016**, *75*, 3. [[CrossRef](#)]
48. Keshtegar, B.; Gholampour, A.; Thai, D.-K.; Taylan, O.; Trung, N.-T. Hybrid regression and machine learning model for predicting ultimate condition of FRP-confined concrete. *Compos. Struct.* **2021**, *262*, 113644. [[CrossRef](#)]
49. Cevik, A. Modeling strength enhancement of FRP confined concrete cylinders using soft computing. *Expert Syst. Appl.* **2011**, *38*, 5662–5673. [[CrossRef](#)]
50. Berthet, J.F.; Ferrier, E.; Hamelin, P. Compressive behavior of concrete externally confined by composite jackets: Part B: Modeling. *Constr. Build. Mater.* **2006**, *20*, 338–347. [[CrossRef](#)]
51. Wu, Y.-F.; Zhou, Y.-W. Unified strength model based on Hoek-Brown failure criterion for circular and square concrete columns confined by FRP. *J. Compos. Constr.* **2010**, *14*, 175–184. [[CrossRef](#)]
52. Al-Salloum, Y. Compressive strength models of FRP-confined concrete. *Asia-Pac. Conf. FRP Struct.* **2007**, *1*, 175–180.

53. Wei, Y.-Y.; Wu, Y.-F. Unified stress–strain model of concrete for FRP-confined columns. *Constr. Build. Mater.* **2012**, *26*, 381–392. [[CrossRef](#)]
54. Wu, H.-L.; Wang, Y.-F. Experimental study on reinforced high-strength concrete short columns confined with AFRP sheets. *Steel and Composite Structures. Steel Compos. Struct.* **2010**, *10*, 501–516. [[CrossRef](#)]
55. Cevik, A.; Göğüş, M.; Güzelbey, İ.; Filiz, H. Soft computing based formulation for strength enhancement of CFRP confined concrete cylinders. *Adv. Eng. Softw.* **2010**, *41*, 527–536. [[CrossRef](#)]
56. Tamuzs, V.; Tepfers, R.; Zile, E.; Ladnova, O. Behavior of concrete cylinders confined by a carbon composite 3. Deformability and the ultimate axial strain. *Mech. Compos. Mater.* **2006**, *42*, 303–314. [[CrossRef](#)]
57. Teng, J.; Jiang, T.; Lam, L.; Luo, Y. Refinement of a design-oriented stress-strain model for FRP-confined concrete. *J Compos. Constr.* **2009**, *13*, 269. [[CrossRef](#)]
58. Binici, B. Design of FRPs in circular bridge column retrofits for ductility enhancement. *Eng. Struct.* **2008**, *30*, 766–776. [[CrossRef](#)]
59. Miyauchi, K. Estimation of Strengthening Effects with Carbon Fiber Sheet for Concrete Column. In Proceedings of the 3rd International Symposium on Non-Metallic (FRP) Reinforcement for Concrete Structures, Japan Concrete Institute, Sapporo, Japan, 14–16 October 1997; pp. 217–224.

**Disclaimer/Publisher’s Note:** The statements, opinions and data contained in all publications are solely those of the individual author(s) and contributor(s) and not of MDPI and/or the editor(s). MDPI and/or the editor(s) disclaim responsibility for any injury to people or property resulting from any ideas, methods, instructions or products referred to in the content.